# Real-Time Monitoring of Weather Radar Network Calibration and Antenna Pointing

VALENTIN LOUF[a] AND ALAIN PROTAT[a]

[a] *Australian Bureau of Meteorology, Melbourne, Victoria, Australia*

(Manuscript received 27 September 2022, in final form 5 April 2023, accepted 18 April 2023)

ABSTRACT: We present an integrated framework that leverages multiple weather radar calibration and monitoring techniques to provide real-time diagnostics on reflectivity calibration, antenna pointing, and dual-polarization moments. This framework uses a volume-matching technique to track the absolute calibration of radar reflectivity with respect to the Global Precipitation Measurement (GPM) spaceborne radar, the relative calibration adjustment (RCA) technique to track relative changes in the radar calibration constant, the solar calibration technique to track daily change in solar power and antenna pointing error, and techniques that track properties of light-rain medium to monitor the differential reflectivity and dual-polarization moments. This framework allows for an evaluation of various calibration and monitoring techniques. For example, we found that a change in the RCA is highly correlated to a change in absolute calibration, with respect to GPM, if a change in antenna pointing can first be ruled out. It is currently monitoring 67+ radars from the Australian radar network. Because of the diverse and evolving nature of the Australian radar network, flexibility and modularity are at the core of the calibration framework. The framework can tailor its diagnostics to the specific characteristics of a radar (band, beamwidth, etc.). Because of its modularity, it can be expanded with new techniques to provide additional diagnostics (e.g., monitoring of radar sensitivity). The results are presented in an interactive dashboard at different level of details for a wide and diverse audience (radar engineers, researchers, forecasters, and management), and it is operational at the Australian Bureau of Meteorology.

SIGNIFICANCE STATEMENT: Weather radars, like all instruments, require maintenance and upgrades. Rainfall measurements are highly variable and sensitive to change, and this can lead to inconsistencies within a radar network. Calibration is the process to counteract those inconsistencies. Any calibration requires a fixed standard to which the changed/upgraded radar can be compared. The SCAR calibration framework presented herein makes use of several standards to retrieve a full set of diagnostics about the radar data. We apply these techniques over the entire Australian weather radar network and demonstrate that, by using this integrated approach, absolute calibration can be achieved to within 1 dB$Z$ of reflectivity, antenna pointing can be monitored within 0.1°, and the various measurements of the radars can be quality controlled.

KEYWORDS: Australia; Measurements; Radars/radar observations; Weather radar signal processing

## 1. Introduction

Radars are key meteorological instruments for studying weather and climate processes, evaluating numerical simulations of precipitating cloud systems, or for monitoring and nowcasting hazardous precipitation events. However, a critical contribution of uncertainty to radar-based quantitative precipitation estimates comes from miscalibration (Houze et al. 2004; Wang and Wolff 2009). A bias in reflectivity calibration deteriorates the accuracy of precipitation estimates by an order of magnitude. A 5-dB bias on reflectivity, which is common, significantly impacts estimations of maximum hail size (Warren et al. 2020), and is also a factor 2 on the rainfall rate: 10 mm $h^{-1}$ corresponds to ~39 dB$Z$, and 20 mm $h^{-1}$ is ~44 dB$Z$, using the Marshall and Palmer (1948) $Z$–$R$ relationships. Thus, the consistency of calibration between radars is a prerequisite for efficient and accurate weather monitoring.

The main quantity measured by radars is the radar reflectivity factor $Z_m$ (e.g., Probert-Jones 1962):

$$Z_m(r) = P_r(t) \times \frac{r^2}{C_r}, \tag{1}$$

where $r$ is the radial distance, $P_r(t)$ is the received power at time $t$, and $C_r$ is the so-called radar constant. The radar equation can be written in a simple form as $Z$ (dB$Z$):

$$Z = -10 \log C_r + 20 \log r + 10 \log P_r. \tag{2}$$

The challenge of radar calibration is to estimate this constant $C_r$ for given radar settings and its variations in real time as $C_r$ depends on a wide range of parameters:

$$C_r = \frac{\pi^3 |K_w|^2}{\lambda^2 2^{10} \ln 2} P_t G^2 \theta_h \theta_v c\tau, \tag{3}$$

where $P_t$ is the transmitted power, $c$ is the celerity, $K_w$ is the dielectric factor, $\lambda$ is the wavelength, $\theta_h$ and $\theta_v$ are the antenna apertures in two orthogonal directions, $\tau$ is the pulse length, and $G$ is the receiver gain.

Maintaining a well-calibrated radar system requires regular testing and maintenance of those components of $C_r$. Since this can be both time consuming and costly, there is great value in

*Corresponding author*: Valentin Louf, valentin.louf@bom.gov.au

DOI: 10.1175/JTECH-D-22-0118.1

calibration tests that characterize the system as a whole. Over the years, many radar calibration techniques have been developed: using a fixed target (Atlas and Mossop 1960), solar interferences (Whiton et al. 1976), statistic of high reflectivity gradients (Mueller 1977), ground clutter echoes (Rinehart 1978), or, for dual-polarization radar only, the self-consistency of polarimetric variables (Gorgucci et al. 1992). Joint observations of precipitating systems with spaceborne radars like Tropical Rainfall Measuring Mission (TRMM; Kawanishi et al. 2000), *CloudSat* (Stephens et al. 2002), or Global Precipitation Measurement (GPM; Hou et al. 2014) have gained a lot of interest from the community (e.g., Protat et al. 2011; Schwaller and Morris 2011; Warren et al. 2018; Crisologo et al. 2018; Huang et al. 2022). TRMM and GPM are reported to have excellent calibration, within <1 dB (Kawanishi et al. 2000; Hou et al. 2014; Oki et al. 2020), and thus are suited to be used as reference for comparing against a network of ground radars (Pejcic et al. 2020; Arias and Chandrasekar 2021).

Radar calibration techniques are often used separately. Yet, it is possible to retrieve additional information about calibration changes by combining different calibration techniques, so-called integrated approaches (Vaccarono et al. 2016; Louf et al. 2019; Lee et al. 2021; Pejcic et al. 2022). For example, the sun calibration monitors the radar receiving chain and the antenna pointing using the sun as a natural radio source (Huuskonen and Holleman 2007). The relative calibration adjustment technique (RCA) uses ground clutter reflectivity to accurately monitor the calibration stability of the radar transmitting chain together with the receiving chain (Silberstein et al. 2008). In the case of miscalibration in the radar transmitting chain the ground clutter calibration is unable to detect whether the loss of calibration affects the transmitting or receiving chain. By combining and comparing the sun calibration with the ground clutter calibration, it is possible to retrieve additional information.

In a previous study, Louf et al. (2019) developed an integrated reflectivity calibration technique called Satellite and Clutter Absolute Radar calibration (SCAR) and tested it on 17 years of observations from CPOL, a C-band dual-polarization (DP) research radar located in the tropics (Keenan et al. 1998). SCAR used the RCA, satellite volume matching, and the self-consistency to monitor the reflectivity bias (e.g., Gorgucci et al. 1992; Scarchilli et al. 1996; Ryzhkov et al. 2005). Louf et al. (2019) provided an in-depth analysis and validation of these calibrations techniques and proposed the framework to be used to monitor the calibration of the radar network nationwide. More recently, Lee et al. (2021) used this principle to monitor the South Korean dual-polarization weather radar network by combining the self-consistency technique, ground clutter monitoring, and radar intercomparison to monitor the reflectivity in real time.

However, many new challenges arose when the SCAR framework was applied on the entire Australian weather radar network. Australia has a diverse radar network comprising 67 radars (at the time of writing) from a range of manufacturers and eras. Of these, 17 are S-band radars and the rest are C-band radars, while 18 are dual polarization. In total, there are 20 unique radar types across the network, operating with a variety of gate spacings (from 150 to 1000 m), beam widths (from 0.9° to 2°), scanning strategies (14 or 15 tilts), and volume update frequencies (5, 6, or 10 min). The network is currently being enhanced via the addition of new sites and the upgrading/replacement of many existing radars. Because of the size, diversity, and the ever-changing nature of the Australian weather radar network, the framework SCAR developed originally on a single high-quality research radar had to be significantly modified. Moreover, this is relevant for other such networks, especially the European OPERA network that is also heterogeneous (Huuskonen et al. 2014b; Saltikoff et al. 2019).

In this paper, we present an updated version of the SCAR integrated calibration framework. SCAR has been built to be flexible and robust to changes in the radar network (automatically integrating new radars, or removing decommissioned radars) and also to adjust to the individual radar characteristics. SCAR's flexibility comes from running independently each monitoring technique and then having an automated summary report that works for whichever technique outputs are applicable for each radar.

To monitor $Z_h$, we use updated versions of the RCA (Wolff et al. 2015; Louf et al. 2019; Hunzinger et al. 2020), and the satellite volume-matching techniques (Warren et al. 2018). We have also introduced in SCAR the solar calibration technique that allows for $Z_h$ and antenna pointing monitoring (Huuskonen and Holleman 2007; Altube et al. 2015). For $Z_{DR}$, the zero $Z_{DR}$ in light rain at vertical incidence, also known as birdbath technique, is still used (Gorgucci et al. 1999), alongside a monitoring technique using signal from Bragg scatterers (Richardson et al. 2017b). SCAR also monitors DP moments using the quality control technique from Marks et al. (2011).

The aim of SCAR is to integrate the various calibration results to provide an accurate diagnostic for each radar. Because of the sheer amount of data being processed every day, the diagnostics need to be generated automatically. The automation of the diagnostic summaries is a challenge in itself. How is one to detect changes in noisy time series? How is one to discriminate a change in calibration from an outlier? When should a calibration alert be triggered? How should thes results be communicated effectively to an audience composed of both expert and nonexpert users?

In section 2, the Australian radar network is presented. This section also discusses observations from GPM and the Learmonth Solar Observatory. In section 3, the overall system architecture of the SCAR framework is presented. In section 4, the individual calibration techniques composing SCAR are reviewed, with a focus on the RCA and GPM volume matching techniques as substantial modifications and improvements have been made, and the inclusion of new calibration techniques that were not discussed in Louf et al. (2019). In section 5, the generation of SCAR diagnostics is presented, showing some operational results, and details about the communication of these diagnostics to the users. Section 6 is the conclusions.

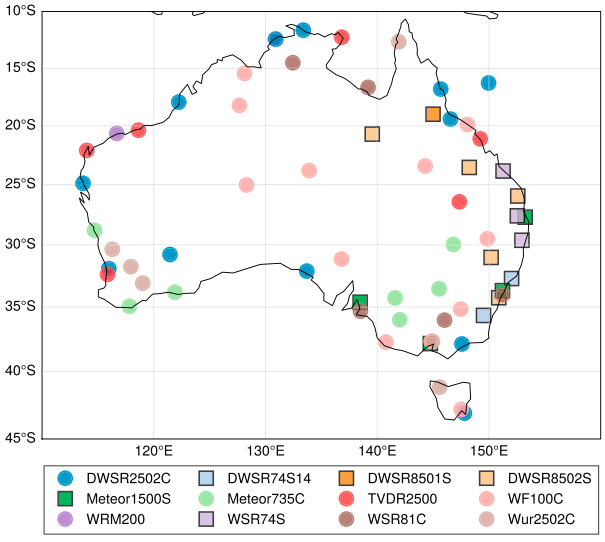


FIG. 1. The Australian weather radar network as of September 2022. S-band radars are represented with a square marker, and C-band radars are represented with a round marker.

## 2. Data

### a. *The Australian weather radar network*

All the weather radars of the Australian Bureau of Meteorology (BOM) network use a standard internal calibration procedure. However, these tests are performed by the radar engineers twice a year at best, due to the remoteness of many of the radars, with no rigorous calibration monitoring the rest of the time. As a result, while exploring the Australian national archive dataset we found abrupt changes in radar calibration, long periods of time where multiple radars are miscalibrated, and large discrepancies between radars with overlapping areas.

Figure 1 shows the Australian weather radar network. The radar network is ranging from the tropics to the midlatitude and is composed of 67 radars at the time of writing, as of August 2022, with plans to add more in strategic areas. These 67 radars have a variety of characteristics (frequency band, beamwidth, manufacturer), resulting in a network with 20 different types of radar. Table 1 shows the different type of radars that are part of the network and some of their characteristics, such as wavelength and beamwidth. Table 1 does not represent the full heterogeneity of the network because the same radar types can have different range resolution, either 125, 250, 500, or 1000 m, or different pulse repetition frequency (PRF), either 250, 400, or 1000 Hz (single or dual PRF), or even number of elevation sweeps per volume (14 tilts for most).

More than 20 radars are in very remote locations of the Australian continent, leading to bandwidth restriction on communication links between these remote radars and the Bureau of Meteorology offices. To save on communication bandwidth, these radars do not return the uncorrected reflectivity to the head office, meaning that techniques using clutter or interferences to track change in calibration are unavailable.

### b. *Spaceborne radar observations*

The GPM satellite carries the Dual-Frequency Precipitation Radar (PR) operating at $K_a$ and $K_u$ bands. The $K_u$-band radar is similar to the PR on TRMM, with a cross-track swath of 245 km. The nominal sensitivity of the $K_u$ PR is 18 dB$Z$, the same as TRMM (Hou et al. 2014); however, prelaunch tests showed that it could detect reflectivities as low as 14.5 dB$Z$ (Toyoshima et al. 2015). GPM data are available since March 2014. Version 7 (released in December 2021) of the 2AKu product is used by SCAR. Note that, hereinafter, when we refer to GPM data we specifically refer to the 2AKu product from the $K_u$-band PR on board the GPM platform.

### c. *Solar observations*

For the solar calibration technique, the sun is used to monitor the alignment and the receiving chain calibration of

TABLE 1. Type of radars in the Australian network. Count represents the number of radars of that type in the network. The wavelength is in centimeters, and the beamwidth is in degrees. Wurrung is an in-house BOM-developed digital receiver system, and all other EEC radars have the previous in-house BOM-developed receivers. DP denotes dual polarization. Note that this table also accounts for three additional radars not yet in operation at the time of writing.

| Type | Count | Wavelength | Beamwidth | Manufacturer | Band |
|---|---|---|---|---|---|
| DWSR 2502C | 4 | 5.3 | 1(3)–1.7(1) | EEC/BOM | C |
| DWSR 74S-14 | 2 | 10.4 | 1.9 | EEC/BOM | S |
| DWSR 8502S-14 | 5 | 10.0 | 1.9 | EEC/BOM | S |
| Meteor 1500S | 4 | 10.0 | 1.0 | Leonardo | S (DP) |
| Meteor 1700S | 3 | 10.0 | 1.0 | Leonardo | S (DP) |
| Meteor 735C | 9 | 5.3 | 1.0 | Leonardo | C (DP) |
| TVDR 2500 | 6 | 5.3 | 1.0(1)–1.9(5) | EEC/BOM | C |
| WF 100–5C | 3 | 5.3 | 1.7(1)–2(2) | EEC/BOM | C |
| WF 100–6C | 10 | 5.3 | 1(2)–1.7(8) | EEC/BOM | C |
| WRM 200–14 | 1 | 5.3 | 1 | Vaisala | C (DP) |
| WSR 74S | 3 | 10.0 | 1.9 | EEC/BOM | S |
| WSR 81C | 3 | 5.3 | 1.0 | EEC/BOM | C |
| Wurrung 2502C | 16 | 5.3 | 1(5)–1.7(11) | EEC/BOM | C |
| MeteopressC-8 | 1 | 5.3 | 1.7 | Meteopress | C (DP) |

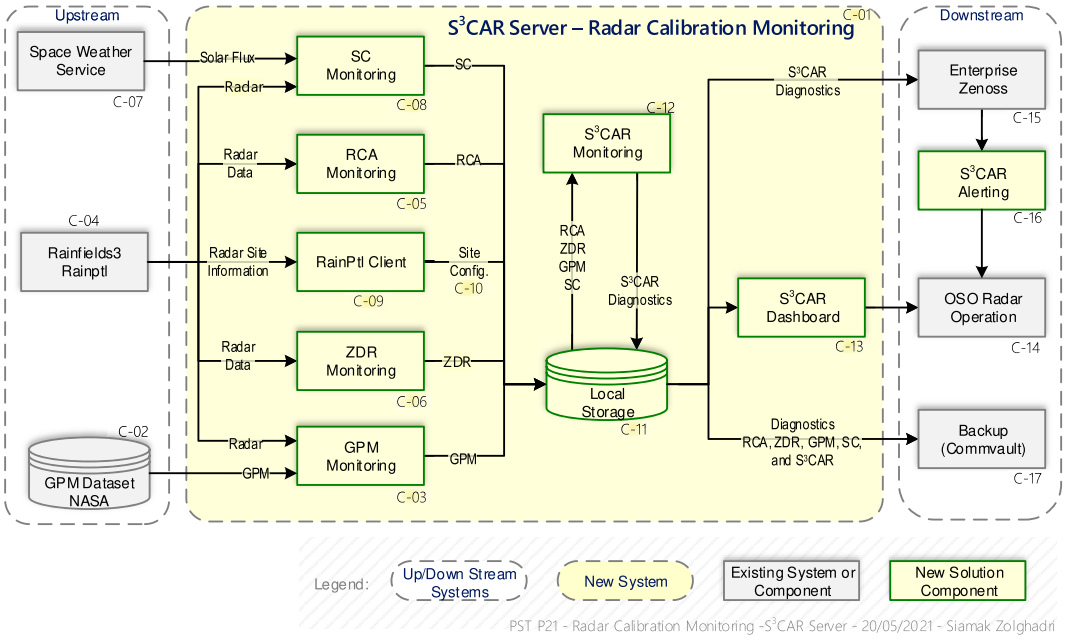


FIG. 2. SCAR system architecture diagram.

the radar antenna. As such, solar flux observations are needed for comparison. The solar flux is continuously monitored at the Learmonth Solar Observatory (22.22°S, 114.10°E) jointly operated by Bureau of Meteorology–Space Weather Services and the U.S. Air Force.[1] A radio telescope with three parabolic dish antennas monitors the solar flux on eight discrete frequencies in the range 245–15 400 MHz. This includes the S and C frequency bands. The solar flux is given in solar flux units: $1\,\text{sfu} = 10^{-22}\,\text{W m}^{-2}\,\text{Hz}^{-1}$.

## 3. The SCAR framework

### a. *Principles and architecture*

Integrated calibration frameworks like SCAR leverage the results of several calibration techniques. Each of these calibration methods have their own advantages and limitations. The RCA can generate a value for every radar volume, but it is only a relative adjustment of the calibration constant $C_r$ [cf. Eq. (2)]. The sun calibration allows monitoring the calibration and sensitivity of the radar receiver, in addition to the antenna pointing accuracy. However, the absolute calibration value is not straightforward and requires comparisons with direct observations of the solar flux. The volume matching of the reflectivity between ground radars and the GPM spaceborne radar gives a unique reference for the whole network. However, the volume-matching technique requires that there be enough precipitation in the ground radar domain during a GPM overpass (1–3 per day), which can lead to several days, sometime weeks, of gap without calibration estimates. It is thus necessary to build a system that can run a variety of techniques with different inputs and analysis windows.

Figure 2 shows the architecture diagram of the SCAR framework. Upstream, we can find the input data sources. The Space Weather Service provides the direct solar flux observations, the BOM operational radar quality control system (Rainfields3) provides the radar data, and NASA provides the GPM data. In yellow is the new system SCAR server that we have built. In Fig. 2, the outputs from SCAR are served downstream to company-wide services like Zenoss for alerting stakeholders on a change in radar calibration.

Rainfields3 converts the data to the OPERA Data Information Model (ODIM) standard format used by European weather agencies (Michelson et al. 2011) and BOM and performs several sets of quality control. One of these quality checks is a beamblocking correction. The beamblocking correction was found by Crisologo et al. (2018) to substantially increase the consistency in the area of overlap between ground radars and GPM observations.

Because each calibration technique has its own requirements, they are run as independent processes. Thus, if one process cannot be run (e.g., some required upstream data are not available) then the other techniques can still run regardless. This also has the advantage that any new calibration method can be implemented in parallel to the others. Each calibration technique is agnostic of the infrastructure, meaning that everything that corresponds to monitoring the directory structure, downloading the data, or publishing the diagnostic is made by processes not related to the calibration technique.

In Fig. 2, upstream data are immediately stored and processed by the different calibration techniques. The upstream

[1] The Learmonth Solar Observatory data are available online (https://www.sws.bom.gov.au/).

radar data are collected every time a new volume is available. This reduces the workload on the system instead of collecting an entire day of data for the entire network at once. The solar calibration (SC monitoring in Fig. 2) and the $Z_{DR}$ monitoring are run every time a new volume is available. Note that SC monitoring is only performed when the sun is below 10° elevation (around sunrise and sunset). Likewise, the $Z_{DR}$ monitoring and dual-polarization QC are only performed for dual-polarization radars. The RCA monitoring first requires a full day of data to generate a clutter mask. It is thus run once a day for each radar (0000 UTC). The GPM monitoring is run whenever a new GPM file is available with the GPM dataset FTP site being checked daily. Because the GPM data can be made available a few days late (in general 2–3 days), SCAR keeps the radar volumes in local storage for a week.

The outputs of the calibration techniques are stored in daily files for each radar except the GPM monitoring technique where it is one file per overpass for each radar, provided sufficient precipitation has been detected.

The self-consistency technique was part of the initial plan in Louf et al. (2019) but was scrapped from production for the operational weather radar network. A problem that we encountered with the self-consistency is that the differential phase $\phi_{DP}$ is encoded as an 8-bit variable (i.e., 256 unique values) going from 0° to 360°. Therefore, $\phi_{DP}$ has a minimal resolution of ~1.4°, which is inadequate for quantitative purposes and thus its monitoring is not useful. This coarse resolution on $\phi_{DP}$ is caused by bandwidth limitation on communication links, and operational $\phi_{DP}$ data are encoded using 8 bits. Moreover, Louf et al. (2019) showed that the self-consistency technique is sensitive to geographical location, which requires disdrometer observations and scattering calculations to derive locally tuned self-consistent relationships between dual-polarization variables. There is no disdrometer currently in operation at the Bureau of Meteorology; thus, the self-consistency is ruled out for now from the set of available techniques in SCAR. However, Louf et al. (2019) detailed the procedure to integrate the self-consistency technique if data requirements were to be met.

### b. *Communicating calibration estimates*

The accurate calibration of the operational radars is an important factor for multiple stakeholders such as severe weather, aviation, forecasters, commercial weather, and public warnings. One of the biggest challenges is to communicate efficiently calibration estimates to a broad audience. The audience of the radar network calibration ranges from the radar engineers who will need to perform tests on the radar site and thus require detailed diagnostics to the forecasters who need to know swiftly if the radar they are using to inform their warnings is running "hot" (positive bias) or "cold" (negative bias). The audience is also composed of researchers using these observations and needing to know the state of calibration for a given period of time and senior leaders within the organization that need to make informed decisions on where to allocate limited resources.

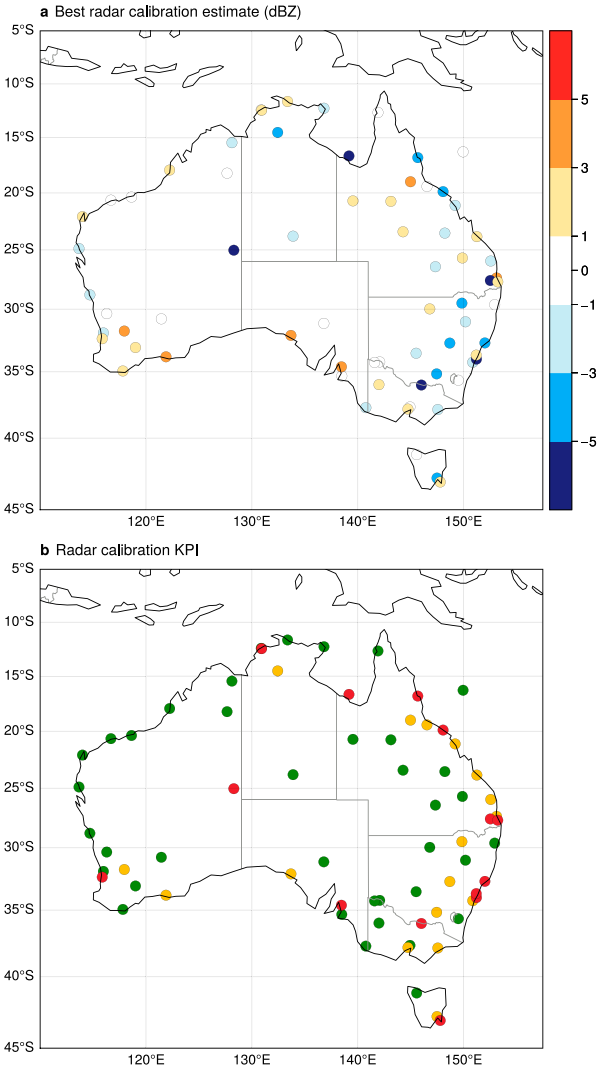


FIG. 3. SCAR dashboard showing (a) the best calibration estimate (dBZ) and (b) the reflectivity KPI for the Australian radar network. The KPI values (red, amber, and green) are shown in Table 3; they depend on the radar tier.

Figure 3 shows the main plot of the SCAR dashboard. The dashboard has three main components: maps of Australia with the radar network (Fig. 3), a summary table of the radar network (Table 2), and a text summary with a list of radars to keep an eye on including a list of radars for which intervention is required. Figure 3a shows the best calibration estimate of the radar reflectivity, i.e., the main result of the SCAR diagnostics. In case a radar does not return the uncorrected reflectivity because of communication link limitation, only the GPM volume-matching technique can be used to assess the calibration. Figure 3b shows the radar calibration key performance indicator (KPI). The KPI index (red, amber, green) depends on the radar tiering. Tier-1 radars are required to have a better calibration accuracy than tier-2 and tier-3 radars of the network (values shown in Table 3). For example, some tier-1 radars can be

TABLE 2. Sample of the SCAR dashboard summary table. The table shows the radar identifier (ID), location name, best calibration estimate (dB), current RCA mean value (dB), elevation and azimuth pointing errors (°), and the radar frequency band, beamwidth (°), and tier.

| ID | Name | Calibration estimate | RCA | Elev error | Azimuth error | Band | Beamwidth | Tier |
|---|---|---|---|---|---|---|---|---|
| 2 | Melbourne | 3.00 | 72.59 | −0.01 | 0.01 | S | 0.91 | 1 |
| 3 | Wollongong (Appin) | −1.00 | 63.06 | 0.11 | 0.03 | S | 1.90 | 1 |
| 4 | Newcastle | −4.00 | 64.70 | 0.12 | 0.00 | S | 2.00 | 1 |
| 5 | Carnarvon | −2.20 | — | — | — | C | 1.60 | 2 |
| 6 | Geraldton | −2.20 | 62.83 | 0.04 | 0.03 | C | 0.95 | 2 |
| 7 | Wyndham | −2.40 | — | — | — | C | 1.70 | 2 |
| 8 | Gympie (Mount Kanigan) | −2.80 | 60.01 | 0.34 | 0.00 | S | 2.00 | 1 |
| 9 | Gove | −1.00 | — | — | — | C | 1.65 | 3 |
| 14 | Mount Gambier | −3.00 | — | — | — | C | 1.58 | 2 |
| 15 | Dampier | 2.40 | 57.75 | 0.12 | 0.16 | C | 0.95 | 2 |
| 16 | Pt Hedland | −1.80 | — | — | — | C | 1.60 | 2 |
| 17 | Broome | 1.60 | 60.06 | −0.17 | 0.02 | C | 1.60 | 2 |
| 19 | Cairns | 2.60 | 60.52 | −0.16 | 0.28 | C | 0.95 | 1 |
| 25 | Alice Springs | −2.60 | — | — | — | C | 1.65 | 3 |
| 31 | Albany | −1.60 | 57.58 | 0.01 | 0.11 | C | 0.95 | 2 |
| 32 | Esperance | −4.80 | 59.02 | 0.01 | 0.02 | C | 0.96 | 2 |
| 33 | Ceduna | 4.20 | 62.93 | −0.11 | 0.18 | C | 1.60 | 3 |
| 38 | Newdegate | −0.80 | 51.96 | 0.12 | 0.13 | C | 1.67 | 2 |
| 39 | Halls Creek | 0.40 | 58.89 | 0.06 | 0.15 | C | 1.60 | 3 |
| 40 | Canberra (Captains Flat) | 0.60 | 67.93 | −0.16 | 0.32 | S | 2.00 | 1 |
| 58 | South Doodlakine | −0.20 | 53.72 | 0.10 | 0.19 | C | 1.67 | 2 |
| 63 | Darwin (Berrimah) | −2.40 | 54.64 | −0.04 | 0.13 | C | 1.00 | 1 |
| 64 | Adelaide (Buckland Park) | 5.00 | 63.23 | −0.05 | 0.04 | S | 0.89 | 1 |
| 66 | Brisbane (Mount Stapylton) | 2.60 | 71.43 | −0.06 | −0.02 | S | 0.89 | 1 |
| 67 | Warrego | −2.60 | — | — | — | C | 1.60 | 2 |
| 68 | Bairnsdale | −0.20 | 59.93 | −0.03 | −0.01 | C | 1.67 | 1 |
| 69 | Namoi | −1.70 | 59.44 | 0.19 | 0.10 | S | 2.00 | 2 |
| 71 | Sydney (Terrey Hills) | 1.20 | 64.32 | 0.04 | 0.06 | S | 0.90 | 1 |
| 93 | Brewarrina | 1.60 | 52.18 | −0.00 | 0.03 | C | 0.92 | 2 |
| 94 | Hillston | −0.60 | 50.50 | 0.00 | 0.02 | C | 0.97 | 2 |
| 95 | Rainbow (Wimmera) | 0.60 | 50.07 | −0.01 | 0.06 | C | 0.90 | 2 |
| 96 | Yeoval | −1.20 | 59.59 | −0.06 | −0.10 | C | 0.96 | 2 |
| 97 | Mildura | 0.20 | 49.04 | 0.01 | 0.03 | C | 0.97 | 2 |
| 98 | Taroom | 2.80 | 61.54 | −0.02 | 0.07 | S | 0.97 | 2 |

on red alert with a reflectivity offset that is close to the value of a tier-3 radar with a green KPI.

The same KPI plot as Fig. 3b is generated for the antenna pointing accuracy (not shown). The azimuth and elevation KPIs are green for an angle offset lower than 0.1°, amber for in between 0.1° and 0.2°, and red for an angle larger than 0.2°. The radar antenna pointing is determined by comparing the predicted position of the sun for a given date, time, latitude, and longitude against the position (azimuth, elevation) of the sun interference in the radar data. At present, some radars (Meteor735C and DWSR2502C-14) have a signal-to-noise ratio filtering that is too high, which filters out most of the sun interference. This should be fixed at a later date for these radars. Unreliable radars appear white on the radar pointing KPI map, which indicates that a diagnostic cannot be produced for this radar. Although the KPI map does not give quantitative results, we found it to be an efficient way to communicate about the quality of the radar network outside of the research, forecast, or engineering teams.

TABLE 3. Key performance indicator index (red, amber, and green) for the radar calibration quality depending on the radar tier.

| Tier | Green | Amber | Red |
|---|---|---|---|
| 1 | $Z_m \leq 1$ dB | $1 < Z_m(\text{dB}) \leq 3$ | $Z_m > 3$ dB |
| 2 and 3 | $Z_m \leq 3$ dB | $3 < Z_m(\text{dB}) \leq 5$ | $Z_m > 5$ dB |

To complement the calibration and KPI dashboards, a table summarizes the diagnostics for all radars (Table 2). The complete one contains all radars in the network. On that table are shown

- the radar identifier (ID) number,
- the radar's location name (the coloration of the name reflects the calibration KPI),
- the best calibration estimate based on a statistically significant number of GPM overpasses [the result should be within ±1 dB according to Protat et al. (2022)],
- the RCA value,
- the elevation and azimuth errors (if the solar interferences are measured),

- the radar band and the radar beamwidth (both parameters influence the solar interferences measurements), and
- the radar tier (the calibration KPI depends on it).

The summary is automatically generated once a day and lists all of the radars and their estimated offset, alongside a green, amber, or red alert.

## 4. Calibration methods

In this section, we present the calibration techniques that compose SCAR. The $Z_h$ is monitored using the RCA algorithm tracking the reflectivity of ground clutter (based on Wolff et al. 2015), the GPMmatch algorithm comparing ground radar to the $K_u$-band radar on board the GPM satellite (based on Warren et al. 2018), and the solar calibration algorithm looking at sun interference to track the antenna pointing and passive measurements of the solar power (Altube et al. 2015). The $Z_{DR}$ is monitored using vertically pointing radar measurements in light rain (Gorgucci et al. 1999), and measurements of Bragg scattering generated by turbulent eddies detected by the radar (Richardson et al. 2017b). Both techniques expect $\overline{Z_{DR}} \approx 0$ dB. The noise level of the dual-polarization moments ($Z_{DR}$, $\rho_{HV}$, $\phi_{DP}$, and $K_{DP}$) are monitored using a set of quality control algorithms adapted from Marks et al. (2011).

### a. *Relative calibration adjustment*

The RCA technique introduced by Silberstein et al. (2008) uses permanent ground clutter around the radar site to monitor $C_r$ [Eq. (3)]. It allows for continuous monitoring of radar health since ground clutter is a persistent radar signature. The RCA technique uses changes in the probability distribution of ground clutter reflectivity to identify changes in the radar system. Because the RCA monitors the calibration using persistent ground clutter, it thus provides a calibration diagnostic, at all time steps, without precipitation, and without intervention. The history of RCA is presented in more detail in Louf et al. (2019).

#### 1) METHODOLOGY

The basis for the RCA technique is that any variation in ground clutter reflectivity is caused by a change in radar calibration constant provided that the elevation and azimuth pointing accuracy does not change. By determining a baseline for the clutter reflectivity ($Z_{c,\mathrm{ref}}$), we can determine the relative calibration offset (Silberstein et al. 2008; Wolff et al. 2015):

$$\mathrm{RCA}_{\mathrm{offset}}\ (\mathrm{dB}) = Z_{c,\mathrm{ref}} - Z_{c,95}, \tag{4}$$

where $Z_{c,95}$ is the 95th percentile of the ground clutter reflectivity distribution, called hereinafter the RCA value. The RCA value is the offset that has to be applied to the reflectivity in order to obtain agreement with the established baseline. The idea of using the 95th percentile of ground clutter reflectivity for monitoring the radar calibration was proposed by Silberstein et al. (2008) and validated by Louf et al. (2019).

The RCA technique can be broken down into two stages. The first is generation of a clutter map to unambiguously identify clutter points. This forms a baseline from which all changes are taken in a relative sense. The second step is to track the RCA value obtained from these clutter points over time and compare it to the baseline. By using other techniques (like GPM volume matching for example), one can determine how far away this baseline is from the absolute calibration.

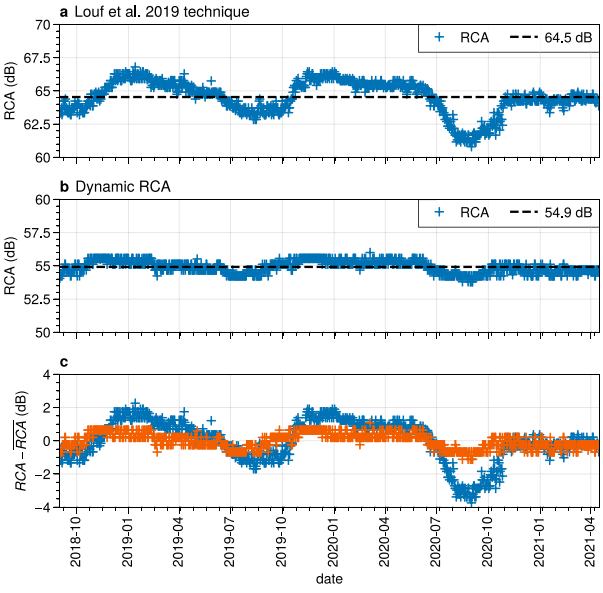


FIG. 4. Time series of RCA values for the South Doodlakine radar (−31.77°N, 117.95°E; Western Australia), a single-polarization C-band radar with a 1.7° beamwidth, using (a) the previous Louf et al. (2019) technique and (b) the dynamic RCA. (c) RCA − $\overline{\mathrm{RCA}}$ for both techniques.

#### 2) DYNAMIC CLUTTER MAP GENERATION

The RCA technique relies on the clutter reflectivity distribution. Thus, the nature of clutter will impact the RCA results. Some radars, near the capital cities, have large areas covered by clutter, including the city itself. Because the scattering properties of building do not vary over time, the RCA is often stable, showing very little variation. However, radars located farther away from cities may have a clutter distribution that is dominated by vegetation with an associated seasonal cycle that can impact the RCA. Because the radar reflectivity of vegetation can vary, their RCA values can show not only seasonal but also diurnal variations. This seasonal cycle is illustrated by Fig. 4, the time series of RCA values for the South Doodlakine radar (−31.77°N, 117.95°E, Western Australia) using (Fig. 4a) the previous Louf et al. (2019) technique, (Fig. 4b) the dynamic RCA described hereinafter. South Doodlakine is a small Western Australian rural location, about 200 km from the capital Perth in the "wheat belt" of Western Australia. The entirety of the clutter map covers crops (there are only 47 residents according to the Australian Bureau of Statistics in that part of the radar domain). The previous Louf et al. (2019) technique considered the clutter map to never change, and they used the same clutter map throughout their 17-yr radar dataset.

Finding a way to mitigate this seasonal cycle caused by vegetation led to the conception of a dynamic composite clutter mask. Hunzinger et al. (2020) proposed an extension of the RCA technique (eRCA) for use with range–height scans and higher-frequency radars in areas with high variability in the clutter field. We have integrated the eRCA clutter map selection method and have made it dynamic to mitigate the high variability of clutter fields with seasonal variability.

The clutter map is developed to determine the statistical distribution of clutter area reflectivity and only uses gate locations that are associated with stable clutter signatures. The following steps are taken to develop the daily clutter mask (Silberstein et al. 2008; Wolff et al. 2015; Louf et al. 2019; Hunzinger et al. 2020):

1) Select all plan position indicators (PPI) scan in a day within 10 km of the radar.
2) Create a fixed polar grid/array with a range–azimuth resolution of 1 km × 1°.
3) Using the 1 km × 1° elements of the fixed polar array, flag each PPI pixel from the lowest tilt that exceeds a specified threshold of reflectivity (45 dB$Z$). Count the number of instances in which this is true for all PPIs in a day.
4) Calculate a percentage of occurrence for each flagged element over the day.
5) The daily clutter map is defined as the range and azimuth locations with an occurrence of more than 80%. All other points are dismissed.

Relative to the eRCA from Hunzinger et al. (2020), the dynamic RCA technique has an extra step in which it accumulates the past 7 days of clutter mask and only keeps gates with an occurrence ≥ 50%.

Figure 4 shows the comparisons between (Fig. 4a) the previous Louf et al. (2019) technique, and (Fig. 4b) the dynamic RCA. The dynamic RCA clearly reduces the variability of the time series compared to the previous RCA technique. The dynamic RCA has a lower mean value with respect to the previous technique; this is because the previous technique only extracted the exact gates flagged by the clutter map, while the dynamic RCA averages raw data to a 1 km × 1° area around identified clutter points. This leads to more data points extracted and thus potentially lower reflectivity points being included in the distribution. Figure 4c shows the RCA and the dynamic RCA offset by their mean value to allow direct comparison between the two techniques. The difference between the maximum and minimum value of the dynamic RCA is 2.2 dB over almost 3 years, while it is 6.0 dB for the previous technique. Moreover, the standard deviation of the dynamic RCA is ±0.4 dB, while the traditional RCA is ±1.2 dB for the same period in Fig. 4.

### b. *Comparison with GPM: GPMmatch*

#### 1) METHODOLOGY

As stated earlier, more than 20 radars are in very remote locations of the Australian continent and do not return the uncorrected reflectivity to the head office to save on communication bandwidth. Thus, the only end-to-end calibration test that can be applied universally on the whole Australian radar network is the satellite volume matching. The volume-matching technique is thus the central tool of the radar reflectivity calibration monitoring framework of the BOM.

The satellite volume-matching method was introduced by Schwaller and Morris (2011) and later refined by Warren et al. (2018). The volume-matching method used in SCAR is a reimplementation of the Warren et al. (2018) technique, with the improvements made in Louf et al. (2019), and is called GPMmatch. Thus, only a short description of the method is given herein and we invite the reader to refer to Warren et al. (2018) for more details.

A major advantage of using a spaceborne radar to calibrate a whole network of radars is that it provides a single source of reference for all ground radars of the network. The overall accuracy of this satellite volume-matching method is thought to be better than 2 dB for individual overpasses (Schwaller and Morris 2011; Warren et al. 2018; Louf et al. 2019). Using collocated weather radar observations between the shipborne OceanPOL radar on the Research Vessel *Investigator* and seven operational radars off the northern and western coasts of Australia (all calibrated with the SCAR framework using GPM), Protat et al. (2022) found that for all seven operational radars, the calibration difference with OceanPOL was within ±0.5 dB, well within the 1-dB requirement for quantitative radar applications.

The GPMmatch algorithm averages over an optimally defined common sampling volume the intersections of ground-based radar and spaceborne radar measurements. The GPMmatch algorithm uses the following steps:

1) Read GPM data and check if a minimum of 10 columns of precipitation measurements from GPM fall within GR domain (if it does the process continues; otherwise, the process stops for the given radar and skips to the next potential ground radar within the GPM swath).
2) Find the ground radar file with the smallest time difference in comparison with the GPM overpass (with a maximum time difference of 300 s).
3) Correct the GPM data coordinates for parallax (Warren et al. 2018).
4) Convert GPM reflectivity data ($K_u$ band) to the ground radar reflectivity band using the dual-frequency ratio (DFR) from Cao et al. (2013) for $K_u$ to S band and the DFR from Louf et al. (2019) for $K_u$ to C band.
5) Start the volume-matching procedure as described in Warren et al. (2018). Warren et al. (2018) advised to work with $f_{min} > 0.7$, $f_{min}$ being the minimum fraction of GR and SR valid data in a volume. We found that a higher $f_{min}$ value reduces the overall variability ($f_{min} > 0.9$); this is close to the 0.95 value originally proposed by Schwaller and Morris (2011).
6) Find the reflectivity offset $\Delta Z$ ($=Z_{GR} - -Z_{GPM}$) between the ground radar and GPM. If $|\Delta Z| > 0.5$ dB, repeat the volume-matching process with the ground radar reflectivity adjusted by $\Delta Z$. Repeat until $|\Delta Z| < 0.5$ dB or until the seventh iteration is reached.

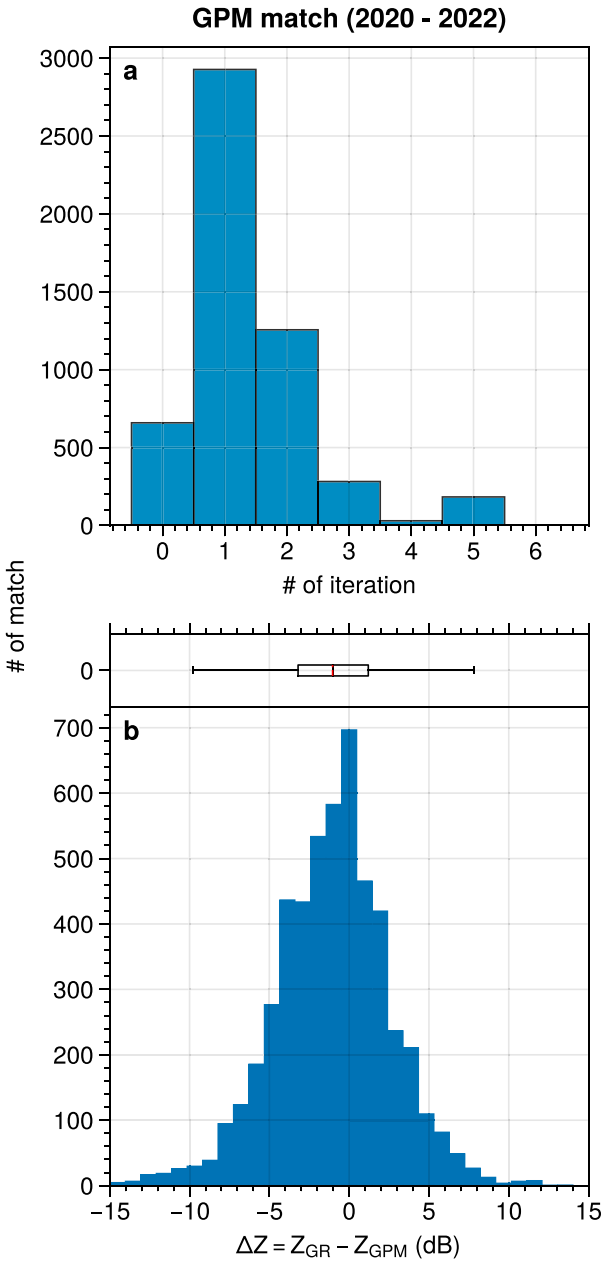


FIG. 5. Histograms of (a) the number of iterations required for the GPMmatch algorithm to find a solution $|\Delta Z| < 0.5$ dB, and (b) the $|\Delta Z|$ final offsets found. The boxplot above the $|\Delta Z|$ histogram represents its interquartile range, median, and mean (in red). The histograms correspond to 5310 matches between GPM and 67 ground radars in Australia between 1 Jan 2020 and 1 Aug 2022.

If the seventh iteration is reached, or $|\Delta Z| > 15$ dB, we consider that the algorithm cannot converge to a solution, and it stops.

Figure 5a shows the number of iterations required for the GPMmatch algorithm to find a solution $|\Delta Z| < 0.5$ dB. Figure 5a shows the importance of the iterative procedure, as the majority of cases (~54%) need at least one iteration, and ~24% of cases needs two iterations to find a solution $|\Delta Z| < 0.5$ dB. There are 342 additional cases, not included in Fig. 5a, that could correspond to a potential failure in the iterative process, or that either the seventh iteration or $|\Delta Z| > 15$ dB is reached.

Figure 5b shows the $|\Delta Z|$ offsets found for the 5310 matches between January 2020 and August 2022 for the entire Australian weather radar network. While the mode of the distribution is located at 0 dB, a slight negative skew is observable.

By running the GPM volume matching over the whole network, it is noticeable that the most frequent matching occurs at high-latitude sites in the south of Australia. Between 1 January 2020 and 31 December 2021 inclusive, for radars that run continuously during that period, there was an average of 97 matches per radar in the tropics, 65 in the subtropics, 99 in the midlatitudes, and 160 for the island of Tasmania. On average, a midlatitude radar has a match with GPM every week. However, because of the dry season in the tropics, there is strictly no match with GPM observed between the months of May and November during that 2-yr period. During the wet season, a match with GPM occurs on average twice per week in the tropics. These statistics represent the combination of two effects. The first is the longer residence time of GPM at the latitudinal extremes of its orbit. The second is latitudinal variations in precipitation frequency, with precipitation occurring more often in the midlatitudes and tropics and less often in the subtropics.

### 2) PERFORMANCE OF THE GPM COMPARISONS

To illustrate the volume-matching comparisons with GPM, the ground radars of Melbourne and Darwin, Australia, are chosen. They are in different climate regimes, Melbourne being in the midlatitudes and Darwin in the tropics. Melbourne radar is a Meteor1500S (cf. Table 1) S-band radar updated (i.e., the existing radar was upgraded to dual polarization by adding a second receiving channel) in the fall of 2017 and Darwin is a DWSR2502C-14 C-band radar updated in July 2015. Because of the frequency differences, we are able to judge the impact that the C-band attenuation can have on the comparison.

Figure 6 shows the volume-matching comparison of the reflectivity offset ($\Delta Z$) from September 2020 to January 2023 between GPM and the ground radar of Melbourne (Fig. 7 for Darwin). These figures are made without any threshold or filter applied to the data. This corresponds to 97 valid GPM overpasses for Melbourne (137 for Darwin), meaning that enough precipitating profiles are detected within the collocated domain of both instruments to perform the volume matching. $\Delta Z = \overline{Z_{GPM} - Z_{GR}}$ is compared with several parameters related to the reflectivity, the spatiotemporal distribution of precipitation, and the geometry of the measurements in both Figs. 6 and 7: the volume-matched GPM and ground radar reflectivity (Figs. 6a, 7a and Figs. 6b, 7b, respectively), the time difference between the ground radar and GPM measurements (Figs. 6c, 7c), the standard deviation of GPM and the ground radar reflectivity inside the matched volume (Figs. 6d, 7d and Figs. 6e, 7e, respectively), the altitude above ground level (AGL) (Figs. 6f, 7f), the

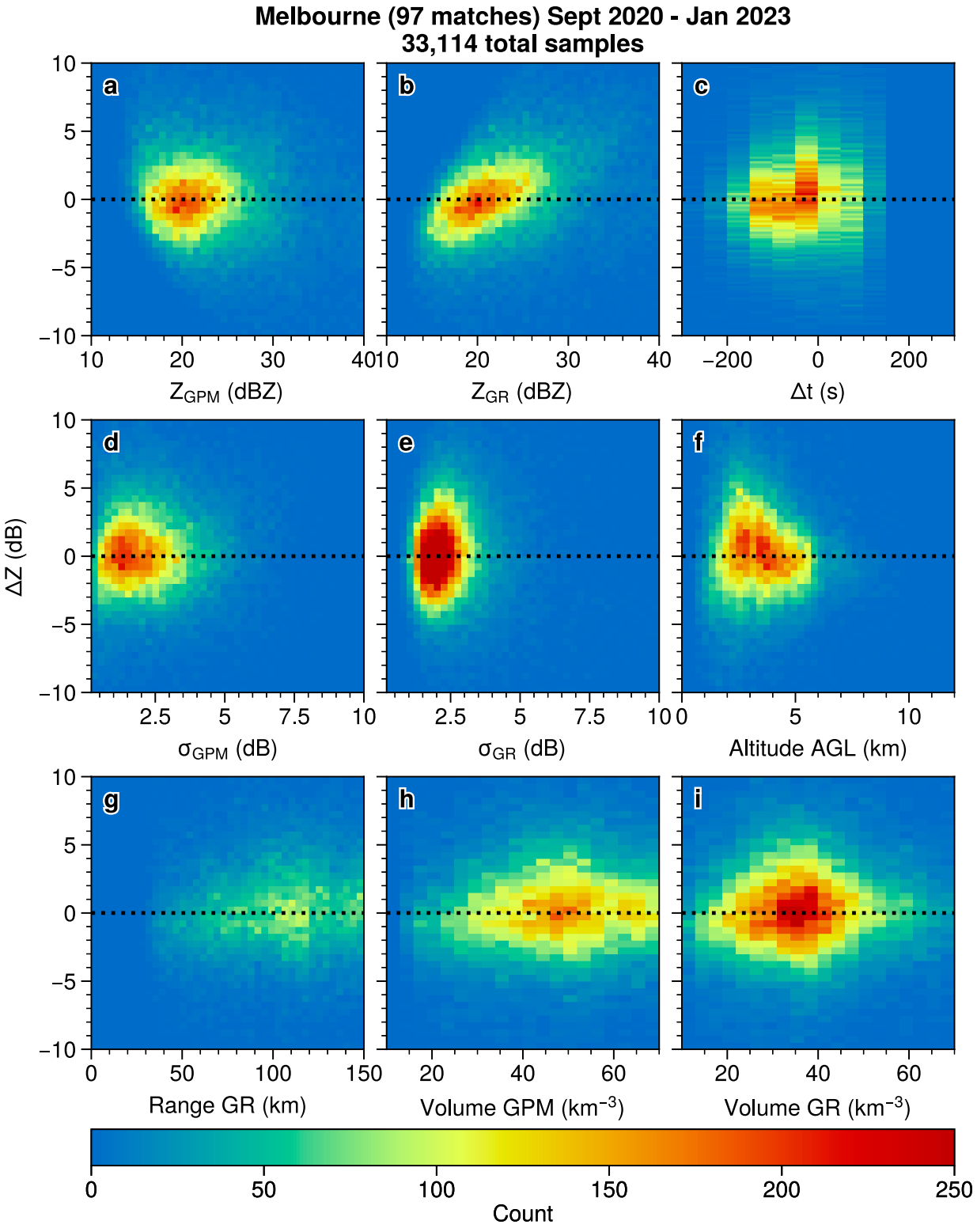


FIG. 6. Bivariate histograms for Melbourne S-band radar of the reflectivity offset $\Delta Z = \overline{Z_{GPM} - Z_{GR}}$ as a function of (a) the volume-matched GPM reflectivity, (b) the volume-matched ground radar (GR) reflectivity ($Z_{GR}$), (c) the time difference between the GR and GPM measurements, (d) the standard deviation of GPM ($\sigma_{GPM}$) reflectivity of the volume matched, and (e) the standard deviation of GR reflectivity ($\sigma_{GR}$), (f) the altitude above ground, (g) the range with respect to the GR, (h) the volume of each individual sample of the GR, and (i) the volume of each individual sample of the GR.

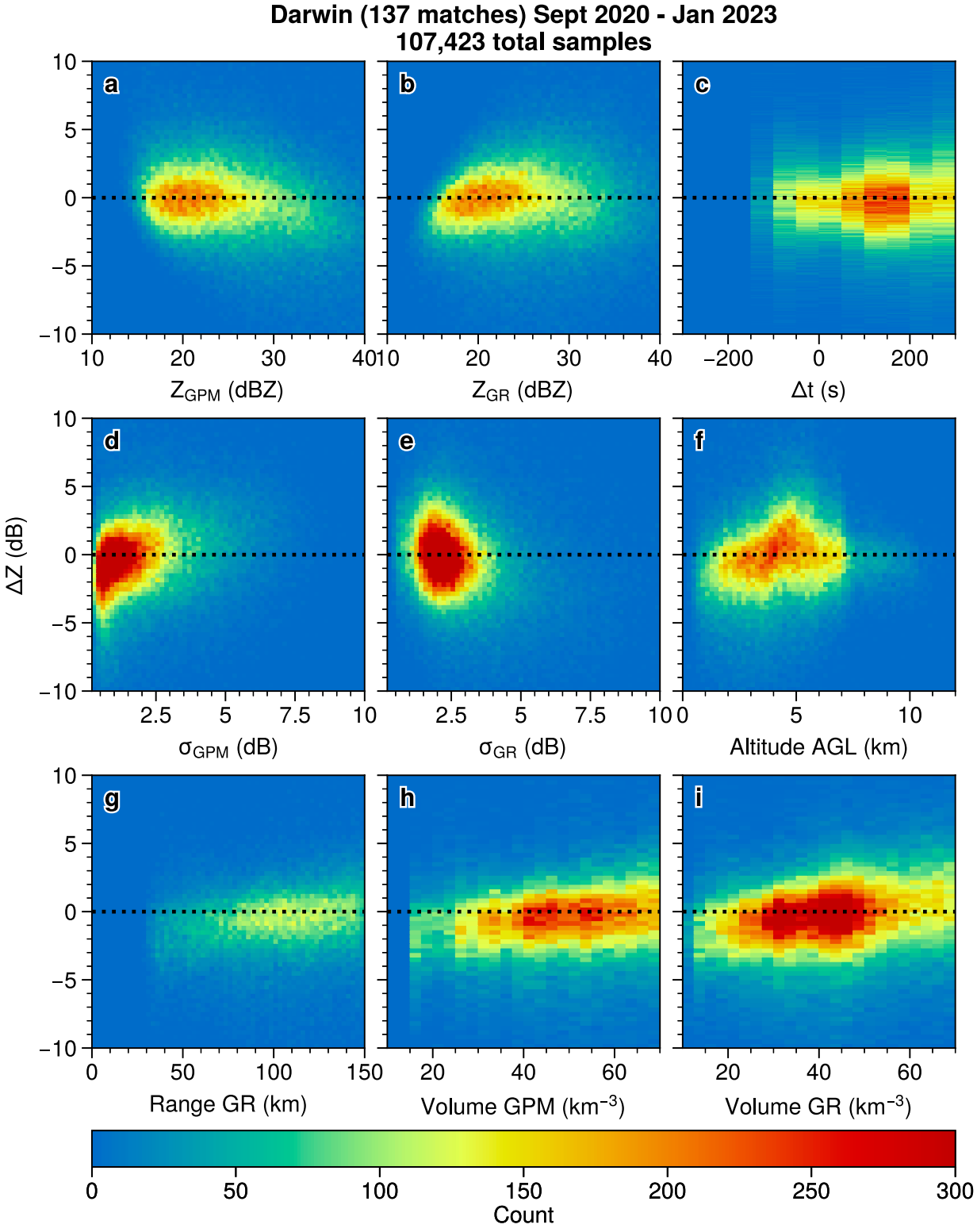


FIG. 7. As in Fig. 6, but for the Darwin C-band DP radar (−12.42°N, 130.89°E).

range with respect to the ground radar (Figs. 6g, 7g), and finally, the matched volume size of GPM and the ground radar (Figs. 6h, 7h and Figs. 6i, 7i, respectively).

Both Figs. 6 and 7 clearly show that $Z_{GPM}$ (Figs. 6a, 7a) and $Z_{GR}$ (Figs. 6b, 7b) have the most significant impact on the resulting reflectivity offset ($\Delta Z$), as expected. There is an unequivocal artifact in Figs. 6b and 7b impacting low values of reflectivity and introducing a bias on $\Delta Z$. This bias is discussed thoroughly in Warren et al. (2018) and is caused by the spaceborne PR sensitivity. Warren et al. (2018) recommended using a minimum threshold value of $Z_{GR} > 21$ dB$Z$ using both TRMM and GPM (their samples were dominated by TRMM comparisons due to the analysis period considered from 2009 to 2015). However, because GPM is more sensitive than its predecessor (Toyoshima et al. 2015), this threshold can be lowered to $Z_{GR} > 18$ dB$Z$ (Figs. 6b and 7b).

Moreover, Fig. 7 shows the clear impact of C-band radar attenuation for high reflectivity values (Figs. 7a,b), with the tail end of the distribution going down, which is absent from the S-band radar data (Figs. 6a,b). For this reason, reflectivities $Z_h > 36$ dB$Z$ are excluded from the volume-matching comparisons (similar as Warren et al. 2018). Note that this threshold in Warren et al. (2018) was driven by potential attenuation errors in the TRMM/GPM measurements.

The time difference between the GR and GPM measurements (Figs. 6c and 7c) does not seem to systemically impact $\Delta Z$ (within the maximum accepted $\Delta t < 300$ s), although the variability does slightly increase when the measurements are farther apart in time (consistent with Schwaller and Morris 2011; Warren et al. 2018). Furthermore, the standard deviation of GPM and GR reflectivity (Figs. 6d, 7d and Figs. 6e, 7e, respectively) within a common matched volume do not seem to have an impact on $\Delta Z$. The only noticeable thing is that $\Delta Z$ is the most variable where the distribution of $\sigma_{GPM}$ and $\sigma_{GR}$ peaks. This is probably because with more samples we are more likely to capture the tails of the distribution.

The altitude above ground level (Figs. 6f and 7f) is where the most significant differences between Melbourne and Darwin are found. Indeed, we can see a net positive bias on $\Delta Z$ around 4.5 km of altitude in Darwin. This is clearly the level of the brightband layer in Darwin. Because the altitude of the bright band in Melbourne varies much more, its effect on $\Delta Z$ are not readily observable in Fig. 6f. However, Fig. 6f shows noticeable variations that could be attributed to brightband effects. Figure 7f clearly indicates that the bright band should be excluded from the volume-matching comparison. This is consistent with findings by Warren et al. (2018), while Schwaller and Morris (2011) advocated to a more conservative position of using samples only above the melting level.

Range of measurements away from the GR (Figs. 6g and 7g), and size of the sampling volume for GPM and GR (Figs. 6 and 7h,i, respectively) do not seem to have an impact on the comparisons.

All the results shown in Figs. 6 and 7 are similar to the studies of Warren et al. (2018) and Huang et al. (2022).

### c. Solar calibration

The third technique used in SCAR is the solar calibration technique, which is a faithful implementation of the Altube et al. (2015) method, with additional corrections for a possible levelling error of the radars as described in Curtis et al. (2021). The solar calibration technique using the sun as a radio source was first proposed by Whiton et al. (1976) and developed in several works by Huuskonen and Holleman (2007), Gabella et al. (2014), and Altube et al. (2015), among others. It allows for monitoring the receiving chain calibration and the alignment of the radar antenna.

In contrast to the sun-tracking technique, which requires dedicated solar scans, the method proposed by Huuskonen and Holleman (2007) can be performed without interrupting the operational scanning sequence. The solar calibration seeks the solar rays intercepted during the operational scanning (the solar interferences). The position of the sun is computed theoretically at the radar location using standard formulas (WMO 2018). The sun position is then converted into azimuth and range bins. As noted by Altube et al. (2015), to achieve an accuracy of 0.1° in sun pointing, given the maximum local speed of the sun across the sky, the interference detection time needs to be accurate within 8–10 s. Furthermore, only interference radials located within ±5° from the actual solar position are considered. This criterion establishes the maximum antenna pointing offset detectable by the method.

Because of the effect of atmospheric refraction, the true sun elevation $\theta_t$ can differ significantly form the observed solar elevation (the apparent elevation $\theta_a$). The radiation of the sun is corrected for refraction using (Holleman and Huuskonen 2013)

$$\tau_t(\theta_t) = \frac{k-1}{2k-1}\cos\theta_t\left[\sqrt{\sin^2\theta_t + \frac{4k-2}{k-1}(n_0-1)} - \sin\theta_t\right], \tag{5}$$

where $k$ is the $k$-model constant and $n_0$ is the refractive index at the Earth surface. The apparent elevation is thus $\theta_a = \theta_t + \tau_t(\theta_t)$. Holleman and Huuskonen (2013) recommended the value of 5/4 for the $k$-model constant and a surface refractivity of 313. Given these conditions, the maximum accuracy error is estimated to be 0.1° (Holleman and Huuskonen 2013).

The estimated solar power $P_{Sun}$ (W) received by the radar is

$$P_{Sun} = 0.5 \times 10^{-13}\Delta f A F, \tag{6}$$

where $\Delta f$ is the bandwidth of the radar receiver (MHz), $A$ is the effective area of the antenna (m$^2$), and $F$ is the solar flux (sfu) measured by Learmonth observatory. The factor 0.5 takes into account the unpolarized nature of the solar radiation, while the radar separately receives the horizontal and vertical polarized components of the incoming radiation. The estimated received solar power is compared with the solar power measured by the radar ($P$; dBm). The solar power is computed by the radar equation from the radar reflectivity measured:

$$P(r) = Z(r) - 20\log(r) - 2\int_0^R a_{\text{gas}}(r)\,dr - C, \qquad (7)$$

where $Z$ is the reflectivity (dB$Z$), $r$ is the range (km), $a_{\text{gas}}$ is the attenuation due to atmospheric gases (dB), and $C$ the radar constant (dB), that is, the calibration constant.

Considering all range bins farther away than 80 km from the radar site, the median value of their power $P_{\text{det}}$ is calculated and recorded as the characteristic power at the antenna port of the interference radial. The solar power received by the radar can be fit to a theoretical model in which the received power is represented by a Gaussian function following the model proposed by Holleman et al. (2010):

$$P_{\text{det}} = l_{\text{gas}} l_{\text{scan}} P_{\text{TOA}} \exp\left\{-4\ln 2\left[\frac{(x-x_0)^2}{\Delta^2_{C,\text{eff}}} + \frac{(y-y_0)^2}{\Delta^2_C}\right]\right\}, \qquad (8)$$

where $l_{\text{gas}}$ and $l_{\text{scan}}$ are the dimensionless gas attenuation and antenna averaging ($l_{\text{gas}} = 10^{a_{\text{gas}}/10}$), $P_{\text{TOA}}$ is the solar power at the top of the atmosphere, $\Delta_C$ is the vertical antenna-sun convolution, $\Delta_{C,\text{eff}}$ the scanning solar width (the result of the convolution between the width of the sun, the antenna pattern, and the azimuth sampling), $x = \phi_R - \phi_S$, $y = \theta_R - \theta_S$, where $\theta$ is the elevation, $\phi$ is the azimuth, $R$ is the position of the solar spikes in the radar data, $S$ is the actual position of the sun, and $(x_0, y_0)$ are the systemic bias in antenna pointing [more details are found in Altube et al. (2015)].

The solar calibration technique is in practice easy to implement. In short, we estimate the position of the sun, corrected for refractivity [Eq. (5)]; we then extract radial where solar interferences are detected. We keep the radial only if more than 50% of gates contain solar interferences and the standard deviation of the computed power is less than 1 dB. Because most of the radar scans are less than 10° of elevation, we only look at scans when the sun is between −1° and 10° of elevation (Curtis et al. 2021). Then the sun interference reflectivity is converted to solar power using Eq. (7). Finally, the solar power at the top of the atmosphere $P_{\text{TOA}}$ and the systematic antenna pointing biases in azimuth and elevation $(x_0, y_0)$, for the azimuth offset and elevation offset, are the parameters retrieved in the inversion of the theoretical model in Eq. (8).

Figure 8 illustrates the relative positions of sun interferences for the Melbourne radar (Fig. 8a) and the Newdegate radar (Fig. 8b). The observations are plotted by the relative position between the interference radial, as given by antenna readings, and the sun. For the Melbourne radar, the antenna pointing has been accurate relative to the sun (Fig. 8a) over the whole SCAR record for this radar, with $\Delta\phi = 0.0° \pm 0.03°$ and $\Delta\theta = 0.0° \pm 0.06°$. For the Newdegate radar, the last change in antenna pointing occurred on 2 May 2020 for the azimuth and on 17 January 2021 for the elevation. The estimated azimuth and elevation pointing errors are $\Delta\phi = 0.13° \pm 0.06°$ and $\Delta\theta = 0.37° \pm 0.08°$, respectively (Fig. 8b).

The solar calibration is performed on $Z_h$. The $Z_{\text{DR}}$ values are also extracted when available, but the algorithm described in Huuskonen et al. (2016) to inverse the model and retrieve the $Z_{\text{DR}}$ values of solar signals is not yet implemented in SCAR. Similarly, the monitoring of the apparent radar beamwidth described in Huuskonen et al. (2014a) could also be applied in SCAR. As for the solar flux method, while we do

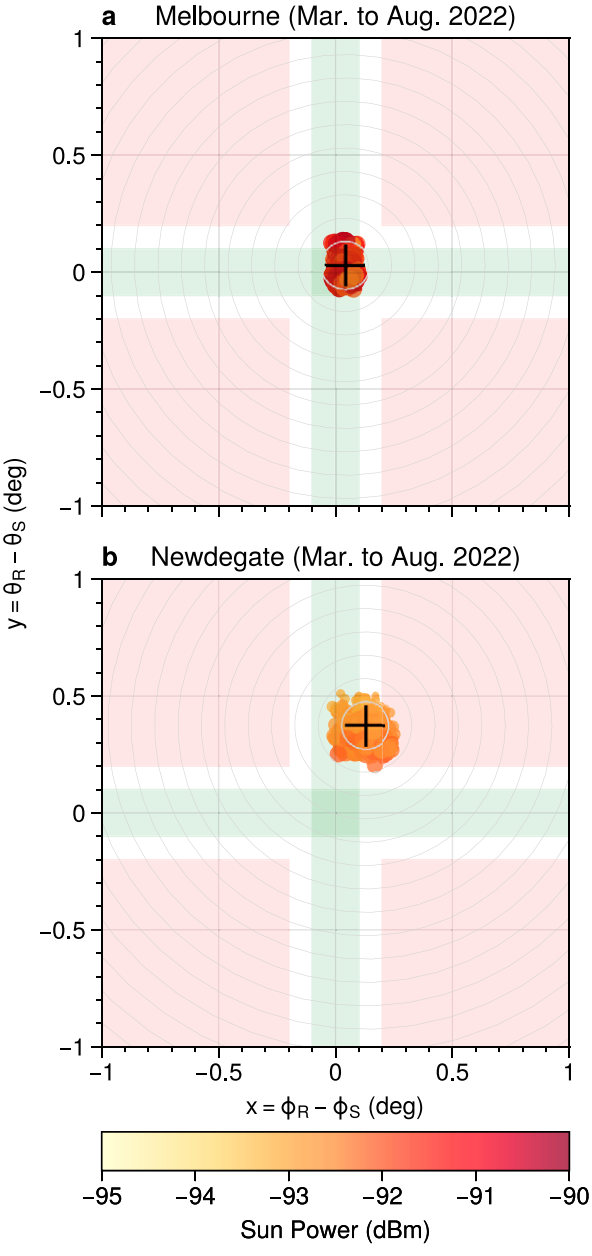


FIG. 8. Relative positions of sun interferences collected by (a) the Melbourne radar (−37.69°N, 144.94°E) and (b) the Newdegate radar (−33.09°N, 119.0°E) for the period from March to August (included) 2022; $\theta$ is the elevation, $\phi$ the azimuth, and the $R$ and $S$ subscripts stand for radar and sun, respectively. The observations are color coded as a function of the detected power (dBm), corrected for atmospheric attenuation. The cross marker is the average relative position for that period. The background green shading is to indicate acceptable values for azimuth/elevation offset (green KPI); the red shading corresponds to the red-alert KPI.

have direct solar observation from the Learmonth observatory, it requires nonstandard metadata that are not available for all of the radars in the BOM network, but it could be readily integrated. These are further improvements to be made to the implementation of the solar calibration technique in SCAR.

### d. Monitoring $Z_{DR}$

The $Z_{DR}$ is a measurement returned only by dual-polarization radars and is indicative of the particle shape and orientation. This opens the possibility of using $Z_{DR}$ in conjunction with $Z_h$ for a better estimate of rainfall by reducing the uncertainty associated with the drop size distributions (Fabry 2015). As a consequence, a bias on $Z_{DR}$ impairs visual interpretation and impacts negatively radar retrievals. Bringi et al. (1983) have determined that $Z_{DR}$ accuracy should be around ±0.2 dB for quantitative application, especially quantitative precipitation estimations (QPE).

Existing methods to calibrate $Z_{DR}$ measurements rely on the intrinsic values of the $Z_{DR}$ of natural targets (e.g., drizzle or dry snow) collected at high elevation angles (e.g., higher than 40° or when possible at 90°, a so-called birdbath), in which $Z_{DR}$ values close to 0 dB are expected. Not all weather radar systems can scan at such high elevation angles, and other methods had to be developed (Sanchez-Rivas and Rico-Ramirez 2022). While studying clear-air Bragg scatterers (at low elevations), Melnikov et al. (2011) noted that "the intrinsic 0 dB of Bragg scatterers can be used for verifying of $Z_{DR}$ radar calibration." More recently, Richardson et al. (2017b) demonstrated the viability of using clear-air Bragg scatterers to estimate the $Z_{DR}$ bias.

Clear-air Bragg scatterers are refractivity gradient returns generated by turbulent eddies detected by weather radars. Because of the randomly oriented nature of the eddies, it results in a $Z_{DR}$ value near 0 dB. Richardson et al. (2017a,b) described in details the theoretical process and the procedure behind this method. The algorithm uses the following steps to calculate an estimate for $Z_{DR}$ bias:

1) Use volumetric data and sample them using the following spatial limits to avoid contamination from ground clutter: $10 < r$ (km) $< 80$ and an elevation angle between 2.4° and 4.5°.
2) Keep samples with reflectivity $Z_h < 10$ dB$Z$, signal-to-noise ratio SNR $< 15$ dB), and cross correlation coefficient $\rho_{HV} \geq 0.98$ to isolate radar range gates associated with Bragg scatterers. Bragg scatterers are usually 0 dB$Z$ or less.
3) Exclude samples with Doppler velocity ($|v| < 2$ m s$^{-1}$), and spectrum width ($\omega < 0.5$ m s$^{-1}$) to avoid clutter. Clutter is often characterized with $v$ and $\omega$ close to 0 m s$^{-1}$.
4) Apply statistical filters (range gate count $> 10\,000$ and interquartile range $< 0.9$ dB) applied to the $Z_{DR}$ distribution to ensure adequate samples for statistics and test for excessive contamination, respectively.
5) Keep only the data with a 90th percentile of reflectivity of ≤3.0 dBZ, to filter out potential precipitation.
6) If the statistical and precipitation filters are passed, then the mode of the $Z_{DR}$ distribution is the $Z_{DR}$ bias.

These filters were chosen to isolate Bragg scatterers (Melnikov et al. 2011; Richardson et al. 2017b). Note that Melnikov et al. (2011) have a different threshold on SNR (SNR $> -7$ dB) when compared with Richardson et al. (2017b) (SNR $< 15$ dB). Melnikov et al. (2011) noted that their threshold on SNR is the minimum possible value returned by their system. They also noted that because Bragg scatterers $Z_{DR} \approx 0$ dB and $\rho_{HV} \approx 1$, coherent summation of signals from the horizontal and vertical receiver channels can add as much as 3 dB to the signal-to-noise ratio. Thus, we decided to use Richardson et al. (2017b) thresholds, with no lower limit on the SNR (just the minimum available) and an upper limit that is slightly above the reflectivity threshold. Because Bragg scatterers can be observed more often relative to the requirements of the $Z_{DR}$ birdbath, this method is a helpful supplement in estimating the $Z_{DR}$ bias.

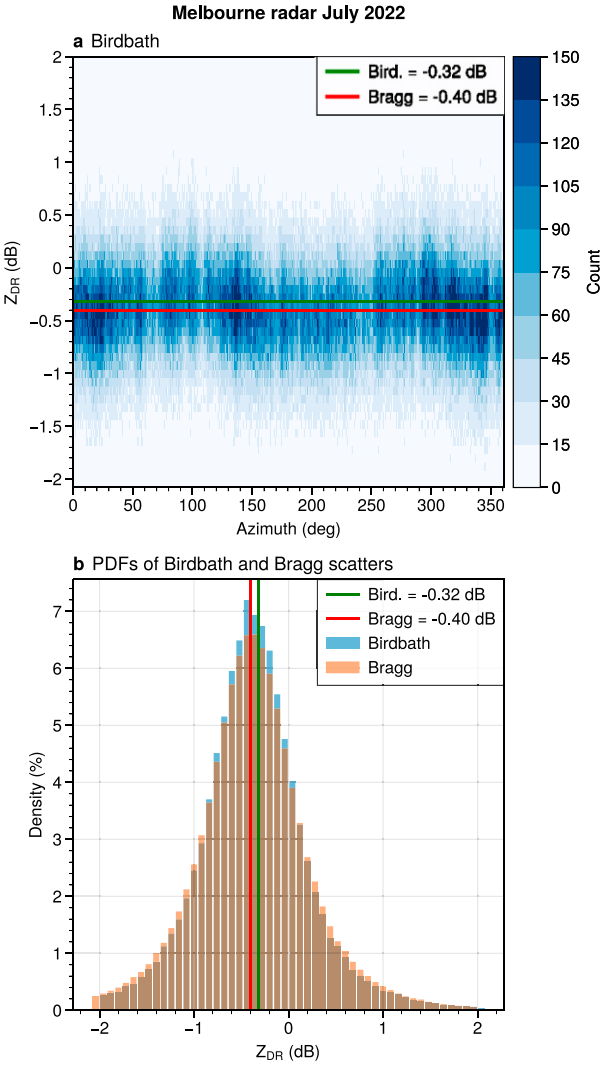


FIG. 9. Differential reflectivity offset for the Melbourne radar in July 2022 using (a) the birdbath method as a function of the azimuth and (b) the normalized probability density function of the birdbath and the Bragg scatterers methods. The red and green lines represent the average $Z_{DR}$ offset found with each method.

Figure 9 illustrates the results for the Melbourne radar during the month of July 2022 of (Fig. 9a) the histogram of the

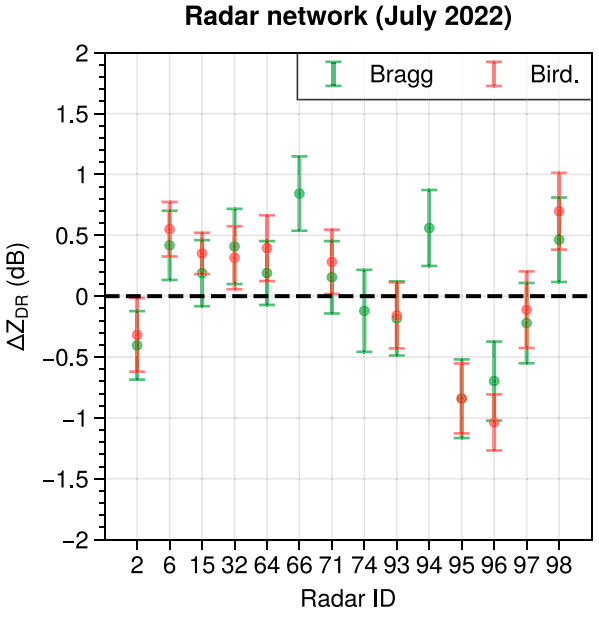


FIG. 10. Comparison between the birdbath method (red) and the Bragg scatterers method (green) to monitor the $Z_{DR}$ bias for all DP radars in the Australian network [denoted by their radar identifier (ID) on the $x$ axis]. The error bars represent the standard deviation around the mean value.

birdbath method as a function of azimuth, and (Fig. 9b) the normalized probability density function of the $Z_{DR}$ bias for the birdbath and Bragg scatterers methods. The birdbath scans, which are performed every 5 min, are part of the volumetric scan. The birdbath method found a $Z_{DR}$ bias of $-0.33 \pm 0.3$ dB using $3 \times 10^4$ points while the Bragg scatterers method found a bias of $-0.40 \pm 0.28$ dB using $8.6 \times 10^4$ points. While Louf et al. (2019) were able to use the birdbath technique to calibrate the CPOL research radar with an accuracy better than 0.2 dB using only a week of data, here the data generated by the Melbourne radar are noisier and do not allow us to be better than 0.3 dB with a month of data. Moreover, the $Z_{DR}$ distribution of Bragg scatterers is well-defined and gives an unambiguous result for the $Z_{DR}$ bias compatible with the results of the more conventional birdbath technique (Fig. 9b).

Figure 10 compares the $Z_{DR}$-birdbath and the Bragg scatterers method for all of the DP radars nationwide. Radars 66 (Mount Stapilton, −27.71°N, 153.24°E), 74 (Greenvale, −18.99°N, 144.99°E), and 94 (Hillston, −33.55°N, 145.52°E) have $Z_{DR}$-Bragg measurements (green) but no associated $Z_{DR}$birdbath measurements (red), because there had been no light rain captured by these radars over that month. This highlights the complementarity of the two techniques. The two techniques otherwise are in agreement within 0.05 dB of each other for the entire network. The standard deviations, averaged over the whole network, are about ±0.3 dB for the Bragg scatterers technique and ±0.26 dB for the birdbath method. Moreover, the variability of the mean individual retrievals are around ~0.2 dB for most radars, which is the accuracy required for $Z_{DR}$ calibration.

### e. *Quality control of the dual-polarization moments*

SCAR dual-polarization quality control is an implementation of Marks et al. (2011) procedure. We invite the reader to refer to Marks et al. (2011, their Fig. 2) for technical details about the process. In short, DP measurements are analyzed in light rain [$20 \leq Z_h$ (dB$Z$) $\leq 28$], as raindrops are spherical with little to no variability in shape, canting angle, or scattering properties within a radar resolution volume (Doviak and Zrnić 2006). Thus, light rain is the perfect medium to use as an indicator of data quality.

To identify suitable data for quality control, Marks et al. (2011) proposed to use the two lowest elevation sweeps, and flag gates with $\rho_{HV} > 0.8$, $-2 \leq K_{DP}$ (° km$^{-1}$) $\leq 3$, $0 \leq Z_{DR}$ (dB) $\leq 2.5$. For each radial, keep sequence of gates with at least 15 consecutive flagged gates where $\sigma(\phi_{DP}) \leq 12°$. From the retained data, the median and the standard deviation of the DP moments are computed and compared against what is expected from light rain (Table 4). Also, Marks et al. (2011) proposed to use the average absolute deviation (AAD) to monitor $Z_{DR}$, as it provides an error measurement in $Z_{DR}$ that is analogous to the root-mean-square error:

$$\mathrm{AAD}(Z_{DR}) = \frac{1}{N}\sum_{i=1}^{N} |Z_{DR}(i) - \overline{Z_{DR}}|, \tag{9}$$

where $N$ is the $Z_{DR}$ is the sample size.

Figure 11 shows the distributions of (Fig. 11a) $\rho_{HV}$, (Fig. 11b) AAD($Z_{DR}$), and (Fig. 11c) $K_{DP}$ for all the dual-polarization radars in Australia for the month of August 2022. For each radar the sample size is between $1.5 \times 10^4$ and $2.5 \times 10^4$. In Fig. 11a, $\rho_{HV} < 0.98$ in light rain is a likely indicator of general radar system issues (Marks et al. 2011). Median $K_{DP}$ measurements should be approximately 0° km$^{-1}$, and average deviation of $Z_{DR}$ from its mean value should be approximately 0 dB (cf. Table 8.1 of Doviak and Zrnić 2006).

Radars 6, 31, 32, and 93 to 98 are all Leonardo Meteor735C C-band radars. They all show similar results for AAD($Z_{DR}$) and $K_{DP}$: close to but slightly above the thresholds in Table 4 (Fig. 11). With the exception of Melbourne, S-band radars show smaller variability and better quality compared to the C-band radars. The poorer performance for Melbourne likely reflects the fact that it is an older radar that was upgraded to dual polarization by adding a second channel.

## 5. SCAR diagnostics

### a. *Integrating the calibration techniques*

After all the monitoring algorithms have processed radar data, once-per-day SCAR diagnostics are generated (cf. Fig. 2). The system produces four diagnostic outputs for each radar: raw time series of the output of all the calibration and monitoring technique available, cleaned time series, automatically generated text messages, and a diagnostic summary of each calibration and monitoring method for the latest available data.

SCAR produces time series that concatenate the median daily values of all the available diagnostics over the past 6

TABLE 4. Expected values of DP moments in light rain. Shown are the median values (with the standard deviation in parentheses) for $Z_h$, AAD($Z_{DR}$), $\rho_{HV}$, $K_{DP}$, and $\sigma(\phi_{DP})$.

| | $Z_h$ (dBZ) | AAD($Z_{DR}$) | $\lvert\rho_{HV}\rvert$ | $K_{DP}$ (° km$^{-1}$) | $\sigma(\phi_{DP})$ |
|---|---|---|---|---|---|
| Light rain | 20–28 | 0 (0.2) | >0.99 (0.01) | 0 (0.1) | <2.5 (<1.0) |

months: GPMmatch, RCA, solar calibration, $Z_{DR}$ birdbath, and $Z_{DR}$ from Bragg scatterers. For radars with communication link bandwidth limitation, that is, that do not return the uncorrected reflectivity, the results of the GPMmatch technique are still available.

The cleaned time series include only the past 180 days of data, while the raw time series contain the data since the start of the system, where the outliers have been excluded. Outliers are removed using an IsolationForest algorithm (Liu et al. 2008). The IsolationForest algorithm is an unsupervised learning algorithm that is used to detect anomalies in data. It works by randomly selecting a feature from the data and splitting the data into two groups based on the selected feature. The algorithm then calculates the average depth of the two groups. If the average depth is small, then the data are considered to be anomalous. In this context, depth refers to the number of steps it would take to get to a leaf node in the decision tree. The average depth is calculated by taking the average of all the depths of the leaf nodes in the decision tree.

The diagnostic summaries are generated by comparing the cleaned time series and the previous day diagnostics. The diagnostics are updated only if the difference compared with the previous diagnostics are above a certain threshold (Table 5). If the diagnostics are updated, then it triggers an alert through

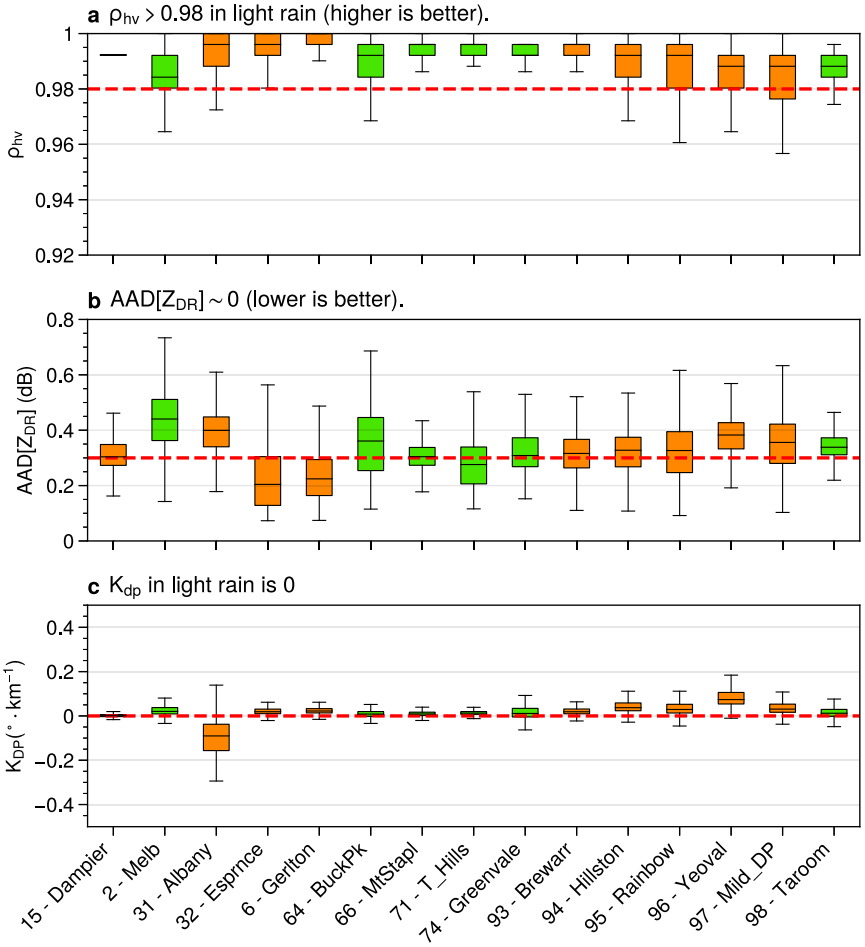


FIG. 11. Distributions of (a) $\rho_{HV}$, (b) AAD($Z_{DR}$), and (c) $K_{DP}$ for all of the dual-polarization radars in Australia for the month of August 2022. The "whiskers" show the three quartile values of the distribution along with extreme values. The red lines denote the acceptable threshold for each moments. The radars are denoted by their ID and short name on the $x$ axis. S-band radars are denoted in green, and C-band radars are in orange.

TABLE 5. Threshold for triggering changes in the diagnostics.

| Diagnostic | Threshold |
|---|---|
| Best calibration estimate | 0.5 dB |
| RCA | 0.25 dB |
| Elev | 0.1° |
| Azimuth | 0.1° |
| Sun power | 0.75 dBm |
| $Z_{DR}$ | 0.2 dB |

Zenoss (a company-wide general-purpose monitoring system) to inform stakeholders of a change in the radar diagnostics.

An important part of the diagnostic summaries is to identify changepoint in the time series. It is a crucial part of the integration of the RCA and the GPM volume matching. We want to average GPMmatch results when and only when the RCA is stable. The stable periods are identified using a segmentation algorithm, robust to signal noise, from the Python package ruptures (Truong et al. 2020).

Figure 12 shows time series of the RCA, solar calibration, and GPMmatch for the Emerald radar located in Queensland. It is an S-band radar with a 2° beamwidth. On 28 January 2021, it became impossible to remotely connect to the KVM switch. Several actions were taken from that date to 23 February 2021. A phase surge protector failed and had to be replaced. The RAPIC transmitter unit was replaced on 10 February 2021. These changes on the hardware caused a large change on the calibration. In Fig. 12, all three radar calibration techniques show a large drop over the same period; however, the magnitude of the change is different. The difference between the first period and the second one is 3.1 dB for the RCA, 13.3 dBm for the solar calibration, and 6.4 dB for the comparison with GPM. Because the three techniques measure different aspect of the radar calibration constant $C_r$ [Eq. (3)], it can be expected that the calibration offset found to be different. In the case of a change of this magnitude, the clutter distribution of the RCA can change significantly, leading to a different ground clutter map, and therefore a new baseline value. It thus becomes crucial for future application of the RCA to identify when a change occurs if it is related to a change in the baseline, or to the calibration constant.

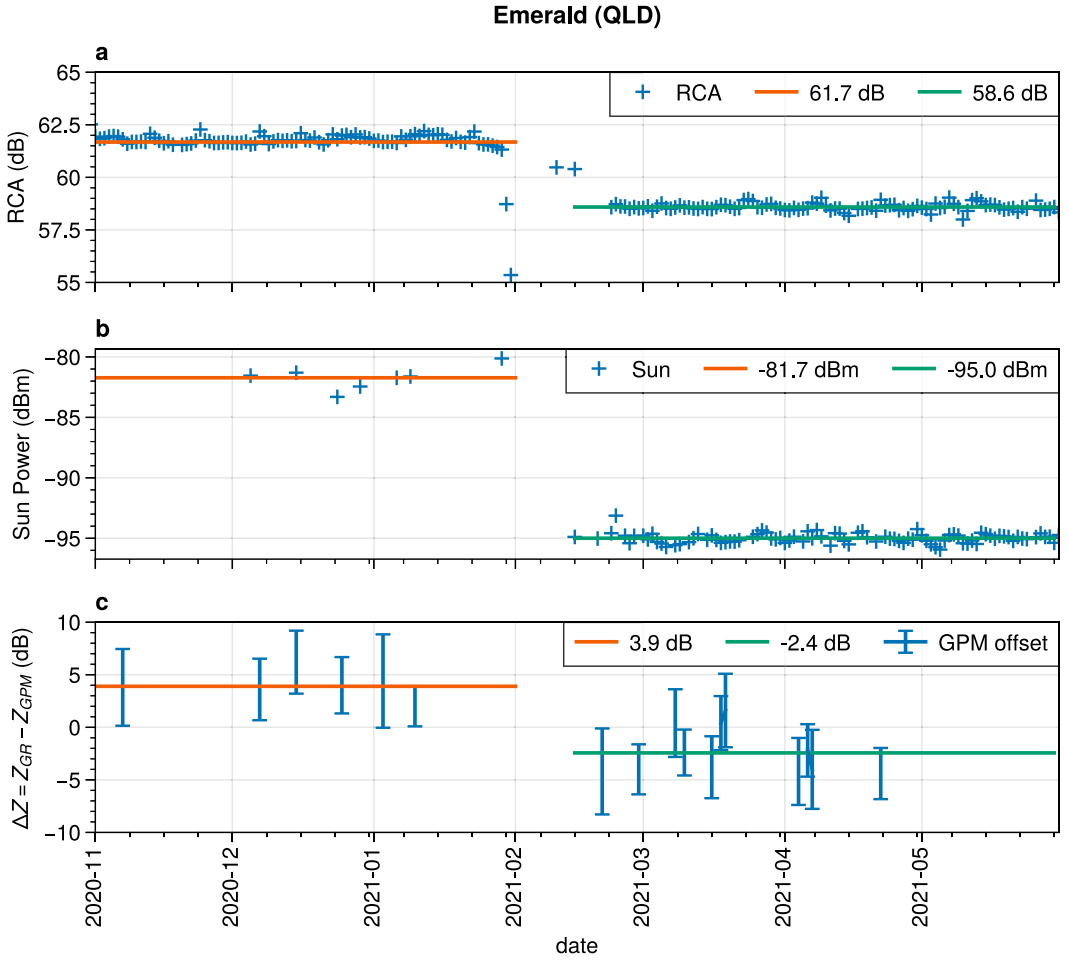


FIG. 12. Time series of (a) RCA, (b) measured solar interferences power, and (c) ground radar bias from GPM, between November 2020 and May 2021 for the Emerald radar (−23.54°N, 148.23°E) in Queensland.

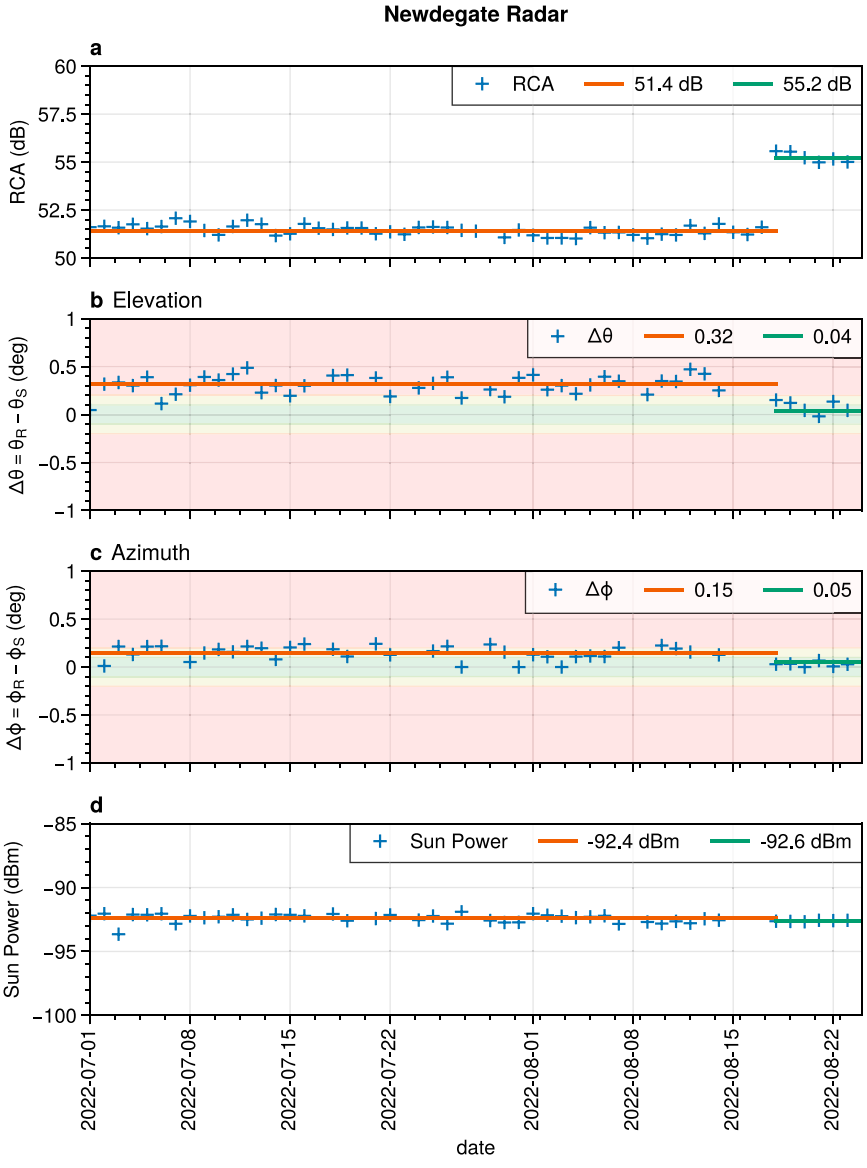


FIG. 13. Time series of (a) RCA, relative position of the sun interference in (b) elevation and (c) azimuth, and (d) detected power of the sun interference for July–August 2022 for the Newdegate radar (−33.09°N, 119.0°E). The orange lines represent the mean values before technical intervention on the radar site to correct the elevation on 17 Aug 2022. The green lines are the mean values after the intervention. Green, amber, and red shadings in (b) and (c) represent the acceptable KPIs for the antenna pointing.

Figure 13 shows time series of the RCA and the solar pointing and calibration for the Newdegate radar located in Western Australia. A BOM radar engineer intervened onsite on 17 August 2022 after looking at the SCAR diagnostics results (cf. Fig. 8). Once he was at the site, he estimated the elevation error to be 0.3° on average, which agrees with SCAR $\overline{\Delta\theta} = 0.32$ (Fig. 13b). Following the correction on the elevation angle, we can see the RCA (Fig. 13a) increased from 51.4 to 55.2 dB. The change in elevation directly impacted the RCA, whereas, as expected, it did not impact the measured solar interference power (Fig. 13b). Thus, the change in elevation did not change the calibration of the radar, but it caused the ground clutter to have a higher reflectivity as the pointing elevation angle of the radar was reduced.

Because of the property of the RCA to change with elevation angle, Lee et al. (2021) used the median value of the ground clutter reflectivity to monitor the antenna pointing. This is made possible in their study as the South Korean weather radar network is sufficiently high-density that overlap between radars allows for intercomparisons of the ground clutter itself. With a network as sparse as the Australian one, it is not a feasible approach. However, the results of Fig. 13 indicate that it is potentially possible.

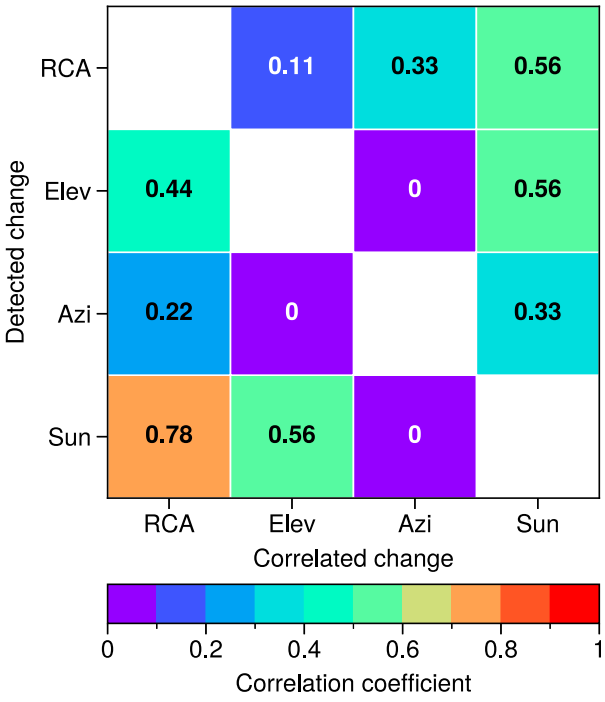


FIG. 14. Correlation map of a detected change in RCA, elevation, azimuth, and sun power and its correlation to these same parameters.

When a shift in the RCA occurs but it is not followed by any change in the offset retrieved with the GPMmatch technique (like in Fig. 13), the procedure is to wait for 5 GPM overpasses after the change in RCA to define a new RCA baseline.

*b. Evaluating the integrated diagnostics*

The initial goal of SCAR was to retrieve additional information about calibration changes by combining different calibration techniques. With SCAR running for almost three years on the entire network, and the automatic change detection allowed by the segmentation algorithm on the time series, it is now possible to verify if the observations made for the cases illustrated by Figs. 12 and 13 are representative. To verify that a given change impacts all of the diagnostics in a consistent manner, we first compute the average values for each segment of the individual time series of each calibration technique for the entire radar network. We then compare the change of value between each segment against the change of value for the other techniques and summarize the results using a Pearson coefficient matrix.

Figure 14 shows the Pearson's correlation coefficient matrix of change in the RCA, the elevation, the azimuth, and the sun power time series and how it relates to a change on these same parameters. Figure 14 is made using the detected changes from the automated segmentation algorithm with a threshold of 0.75 dB (or dBm) for the RCA (or the solar power), and a threshold of 0.1° for the azimuth and elevation, on the diagnostic time series of 40 radars returning the uncorrected reflectivity from 2020 to 2022. The most frequent detected changes are for the RCA with 106 segments, followed by the elevation angle (65 changes), the sun power (60), and the azimuth (57). The GPM volume matching produces less data for the time series compared to the other techniques, and also data that are more variable. This is why we did not estimate the correlation between GPM results and the other diagnostics.

Figure 14 quantifies that a change in one parameter is linked to a change in another. For example, azimuth and elevation are completely independent from one another, so no correlation is expected between these two parameters ($p = 0$). However, a change in sun power correlates at $p = 0.78$ to a change in RCA, while a change detected in RCA correlates to a change in sun power at $p = 0.56$. This is expected, as the RCA measures a change in the radar constant $C_r$ [Eq. (3)], and thus, a change in the elevation, the azimuth, or the sun power is likely to impact the RCA.

As shown in Fig. 13, a change in the elevation for the Newdegate radar caused an immediate change in the RCA of almost 4 dB. Figure 14 shows that a change in the elevation has a $p = 0.44$ correlated change in the RCA. However, if the correlation coefficient between the elevation and the RCA is computed by excluding any change related to the sun power, then $p = 0.87$ between the elevation and the RCA.

To estimate how the GPM results are impacted by the RCA, the $\overline{\Delta Z}$ offset of the volume-matching technique is computed when a change is detected in the RCA. A weak correlation of $p = 0.24$ is found between the two. Nevertheless, if changes in the RCA due to the antenna pointing are excluded, then the correlation between a change in the RCA and the GPM offsets is $p = 0.81$. This result indicates that a change in RCA value associated with a real change in calibration (not a change in pointing accuracy) is indeed detected by the GPM technique as well most of the time.

Overall, the results of Fig. 13 demonstrate that SCAR satisfies the design objective of retrieving additional information about radar calibration using complementarity between techniques.

## 6. Summary and conclusions

In this study, we presented SCAR, an operational integrated radar calibration and quality control monitoring system that runs in real time on the entire Australian weather radar network. The Australian weather radar network is heterogeneous and comprises 20 different types of radars. SCAR integrates the results of multiple calibration and quality control techniques to provide real-time diagnostics for monitoring calibration bias and general radar health checks. As a result, SCAR has become a valuable tool at the Australian Bureau of Meteorology, used by radar engineers to evaluate the radar system during and after regular maintenance, by downstream systems that depend on radar data to correct reflectivity bias (e.g., rainfall), and by forecasters to quickly assess the radar reflectivity bias.

SCAR uses the volume-matching technique with GPM spaceborne radar to track the absolute calibration of radar

reflectivity. SCAR also uses the relative calibration adjustment (RCA) technique to track relative changes in the radar calibration constant and the solar calibration technique to track solar interferences and monitor the antenna pointing error. SCAR monitors $Z_{DR}$ using measurements of Bragg scatterers and birdbath scans in light rain. SCAR also monitors dual-polarization moments ($Z_{DR}$, $K_{DP}$, $\phi_{DP}$, and $\rho_{HV}$) using polarimetric properties of the rain medium.

A major advantage of the GPM volume matching technique is that all radars of the network are calibrated against a single source of reference. The GPM volume matching technique literature (Schwaller and Morris 2011; Warren et al. 2018; Crisologo et al. 2018; Louf et al. 2019; Protat et al. 2022) suggests that errors are of approximately 2 dB from individual GPM overpasses to better than 1 dB when stable periods of calibration can be estimated using the RCA technique and individual GPM estimates can be averaged over this period.

The RCA technique is a useful tool for a posteriori calibration (Silberstein et al. 2008; Louf et al. 2019; Hunzinger et al. 2020). The technique captures changes in calibration as low as ±0.5 dB. For this reason, the RCA technique is used in SCAR as a tool for monitoring the health of the radar. We proposed in this paper the dynamic clutter mask generation to improve the RCA stability when the clutter map is mostly composed of vegetation. We showed that in the presence of a clutter distribution mostly composed of vegetation with strong seasonal effects that impact the RCA value, the dynamic clutter map reduces the seasonal variability from ±4 to ±1 dB.

SCAR also showed that the $Z_{DR}$-Bragg technique results within 0.05 dB of the $Z_{DR}$-birdbath technique. Not all weather radar systems can scan at high elevation angles or point the antenna vertically to collect precipitation measurements passing overhead to monitor $Z_{DR}$ (Sanchez-Rivas and Rico-Ramirez 2022). These results demonstrate that the differential reflectivity of Bragg scatterers at low elevations can be used to calibrate $Z_{DR}$ with the same confidence as the $Z_{DR}$-birdbath technique.

SCAR also uses the detection of the sun to determine the elevation and azimuth biases of the radar antenna and detect potential issues with the radar receiver. This solar calibration method is well established (Huuskonen and Holleman 2007; Altube et al. 2015). SCAR confirms that any changes in antenna pointing will impact the RCA, and thus, both techniques can be used to monitor radar performance as well as engineering changes (e.g., elevation offset). Future work includes the monitoring of the radar sensitivity, the monitoring of transmission–reception limiter issues, and the quantitative intercomparison between radars, where it is possible.

SCAR diagnostics are now ingested in real time in downstream applications like radar-based rainfall, wind, and hail analysis and nowcasting products delivered by BOM to the public and customers. SCAR is a robust framework to monitor more than just the radar reflectivity calibration but the general health of the radar thanks to automated quality control of the data output. However, SCAR as a monitoring tool for an entire network is highly dependent on the data from GPM satellite. If GPM would cease to function and no spaceborne precipitation radars are available anymore, then SCAR would lose the ability to retrieve the absolute reflectivity calibration offset. This provides additional motivation for investment in future spaceborne radar platforms.

*Acknowledgments.* We thank Todd Berendes, Walt Petersen, David Wolff, and David Marks from the Information Technology and Systems Center at the University of Alabama in Huntsville, Alabama, for the automated providing of the Australian continental subset of GPM data. We thank Patricia Altube for providing the code of her work on solar calibration freely on GitHub (https://github.com/paltube/solar_calibration); this was very helpful in designing the Python version of that code that is implemented by SCAR. We thank Karl Achkar, Mark Curtis, Susan Fisher, and Siamak Zolghadri of the Bureau of Meteorology for help on coding and designing the system architecture of the SCAR server. We thank Colin Jenkinson, radar engineer at the Bureau of Meteorology, whose intervention on the Newdegate radar was the incentive to make Fig. 13. Figures in this paper have been made using the ProPlot library (Davis 2021).

*Data availability statement.* The calibration methods presented herein are freely available as open-source (under Apache license, version 2.0) Python libraries: the dynamic RCA (http://www.github.com/vlouf/cluttercal), the satellite volume matching (http://www.github.com/vlouf/gpmmatch), and the solar calibration technique (http://www.github.com/vlouf/suncal).

## REFERENCES

Altube, P., J. Bech, O. Argemí, and T. Rigo, 2015: Quality control of antenna alignment and receiver calibration using the sun: Adaptation to midrange weather radar observations at low elevation angles. *J. Atmos. Oceanic Technol.*, **32**, 927–942, https://doi.org/10.1175/JTECH-D-14-00116.1.

Arias, I., and V. Chandrasekar, 2021: Cross validation of the network of ground-based radar with GPM during the Remote Sensing of Electrification, Lightning, and Mesoscale/Microscale Processes with Adaptive Ground Observations (RELAMPAGO) field campaign. *J. Meteor. Soc. Japan*, **99**, 1423–1438, https://doi.org/10.2151/jmsj.2021-069.

Atlas, D., and S. C. Mossop, 1960: Calibration of a weather radar by using a standard target. *Bull. Amer. Meteor. Soc.*, **41**, 377–382, https://doi.org/10.1175/1520-0477-41.7.377.

Bringi, V. N., T. A. Seliga, and S. M. Cherry, 1983: Statistical properties of the dual-polarization differential reflectivity ($Z_{DR}$) radar signal. *IEEE Trans. Geosci. Remote Sens.*, **GE-21**, 215–220, https://doi.org/10.1109/TGRS.1983.350491.

Cao, Q., Y. Hong, Y. Qi, Y. Wen, J. Zhang, J. J. Gourley, and L. Liao, 2013: Empirical conversion of the vertical profile of reflectivity from Ku-band to S-band frequency. *J. Geophys. Res. Atmos.*, **118**, 1814–1825, https://doi.org/10.1002/jgrd.50138.

Crisologo, I., R. A. Warren, K. Mühlbauer, and M. Heistermann, 2018: Enhancing the consistency of spaceborne and ground-based radar comparisons by using beam blockage fraction as a quality filter. *Atmos. Meas. Tech.*, **11**, 5223–5236, https://doi.org/10.5194/amt-11-5223-2018.

Curtis, M., S. Dance, V. Louf, and A. Protat, 2021: Diagnosis of tilted weather radars using solar interference. *J. Atmos.*

*Oceanic Technol.*, **38**, 1613–1620, https://doi.org/10.1175/JTECH-D-20-0179.1.

Davis, L. L. B., 2021: ProPlot. Zenodo, https://doi.org/10.5281/ZENODO.5602155.

Doviak, R. J., and D. S. Zrnić, 2006: *Doppler Radar and Weather Observations*. Dover Publications, 592 pp.

Fabry, F., 2015: *Radar Meteorology: Principles and Practice*. Cambridge University Press, 276 pp.

Gabella, M., M. Sartori, M. Boscacci, and U. Germann, 2014: Vertical and horizontal polarization observations of slowly varying solar emissions from operational Swiss weather radars. *Atmosphere*, **6**, 50–59, https://doi.org/10.3390/atmos6010050.

Gorgucci, E., G. Scarchilli, and V. Chandrasekar, 1992: Calibration of radars using polarimetric techniques. *IEEE Trans. Geosci. Remote Sens.*, **30**, 853–858, https://doi.org/10.1109/36.175319.

——, ——, and ——, 1999: A procedure to calibrate multiparameter weather radar using properties of the rain medium. *IEEE Trans. Geosci. Remote Sens.*, **37**, 269–276, https://doi.org/10.1109/36.739161.

Holleman, I., and A. Huuskonen, 2013: Analytical formulas for refraction of radiowaves from exoatmospheric sources. *Radio Sci.*, **48**, 226–231, https://doi.org/10.1002/rds.20030.

——, ——, M. Kurri, and H. Beekhuis, 2010: Operational monitoring of weather radar receiving chain using the sun. *J. Atmos. Oceanic Technol.*, **27**, 159–166, https://doi.org/10.1175/2009JTECHA1213.1.

Hou, A. Y., and Coauthors, 2014: The Global Precipitation Measurement mission. *Bull. Amer. Meteor. Soc.*, **95**, 701–722, https://doi.org/10.1175/BAMS-D-13-00164.1.

Houze, R. A., Jr., S. Brodzik, C. Schumacher, S. E. Yuter, and C. R. Williams, 2004: Uncertainties in oceanic radar rain maps at Kwajalein and implications for satellite validation. *J. Appl. Meteor.*, **43**, 1114–1132, https://doi.org/10.1175/1520-0450(2004)043<1114:UIORRM>2.0.CO;2.

Huang, H., K. Zhao, P. Fu, H. Chen, G. Chen, and Y. Zhang, 2022: Validation of precipitation measurements from the Dual-Frequency Precipitation Radar onboard the GPM Core Observatory using a polarimetric radar in South China. *IEEE Trans. Geosci. Remote Sens.*, **60**, 4104216, https://doi.org/10.1109/TGRS.2021.3118601.

Hunzinger, A., J. C. Hardin, N. Bharadwaj, A. Varble, and A. Matthews, 2020: An extended radar relative calibration adjustment (eRCA) technique for higher-frequency radars and range–height indicator (RHI) scans. *Atmos. Meas. Tech.*, **13**, 3147–3166, https://doi.org/10.5194/amt-13-3147-2020.

Huuskonen, A., and I. Holleman, 2007: Determining weather radar antenna pointing using signals detected from the sun at low antenna elevations. *J. Atmos. Oceanic Technol.*, **24**, 476–483, https://doi.org/10.1175/JTECH1978.1.

——, M. Kurri, H. Hohti, H. Beekhuis, H. Leijnse, and I. Holleman, 2014a: Radar performance monitoring using the angular width of the solar image. *J. Atmos. Oceanic Technol.*, **31**, 1704–1712, https://doi.org/10.1175/JTECH-D-13-00246.1.

——, E. Saltikoff, and I. Holleman, 2014b: The operational weather radar network in Europe. *Bull. Amer. Meteor. Soc.*, **95**, 897–907, https://doi.org/10.1175/BAMS-D-12-00216.1.

——, M. Kurri, and I. Holleman, 2016: Improved analysis of solar signals for differential reflectivity monitoring. *Atmos. Meas. Tech.*, **9**, 3183–3192, https://doi.org/10.5194/amt-9-3183-2016.

Kawanishi, T., and Coauthors, 2000: TRMM Precipitation Radar. *Adv. Space Res.*, **25**, 969–972, https://doi.org/10.1016/s0273-1177(99)00932-1.

Keenan, T., K. Glasson, F. Cummings, T. S. Bird, J. Keeler, and J. Lutz, 1998: The BMRC/NCAR C-band polarimetric (C-POL) radar system. *J. Atmos. Oceanic Technol.*, **15**, 871–886, https://doi.org/10.1175/1520-0426(1998)015<0871:TBNCBP>2.0.CO;2.

Lee, J.-E., S. Kwon, and S.-H. Jung, 2021: Real-time calibration and monitoring of radar reflectivity on nationwide dual-polarization weather radar network. *Remote Sens.*, **13**, 2936, https://doi.org/10.3390/rs13152936.

Liu, F. T., K. M. Ting, and Z.-H. Zhou, 2008: Isolation forest. *2008 Eighth IEEE Int. Conf. on Data Mining*, Pisa, Italy, IEEE, 413–422, https://doi.org/10.1109/ICDM.2008.17.

Louf, V., A. Protat, R. A. Warren, S. M. Collis, D. B. Wolff, S. Raunyiar, C. Jakob, and W. A. Petersen, 2019: An integrated approach to weather radar calibration and monitoring using ground clutter and satellite comparisons. *J. Atmos. Oceanic Technol.*, **36**, 17–39, https://doi.org/10.1175/JTECH-D-18-0007.1.

Marks, D. A., D. B. Wolff, L. D. Carey, and A. Tokay, 2011: Quality control and calibration of the dual-polarization radar at Kwajalein, RMI. *J. Atmos. Oceanic Technol.*, **28**, 181–196, https://doi.org/10.1175/2010JTECHA1462.1.

Marshall, J. S., and W. M. K. Palmer, 1948: The distribution of raindrops with size. *J. Meteor.*, **5**, 165–166, https://doi.org/10.1175/1520-0469(1948)005<0165:TDORWS>2.0.CO;2.

Melnikov, V. M., R. J. Doviak, D. S. Zrnić, and D. J. Stensrud, 2011: Mapping Bragg scatter with a polarimetric WSR-88D. *J. Atmos. Oceanic Technol.*, **28**, 1273–1285, https://doi.org/10.1175/JTECH-D-10-05048.1.

Michelson, D. B., R. Lewandowski, M. Szewczykowski, H. Beekhuis, and G. Haase, 2011: EUMETNET OPERA weather radar information model for implementation with the HDF5 file format. EUMETNET Doc., 36 pp., https://www.eumetnet.eu/wp-content/uploads/2019/05/OPERA-ODIM_H5-v2.1.pdf.

Mueller, E. A., 1977: Statistics of high radar reflectivity gradients. *J. Appl. Meteor.*, **16**, 511–513, https://doi.org/10.1175/1520-0450(1977)016<0511:SOHRRG>2.0.CO;2.

Oki, R., T. Iguchi, and K. Nakamura, 2020: The GPM DPR validation program. *Satellite Precipitation Measurement*, V. Levizzani et al., Eds., Advances in Global Change Research, Vol. 69, Springer, 503–514, https://doi.org/10.1007/978-3-030-35798-6_3.

Pejcic, V., P. Saavedra Garfias, K. Mühlbauer, S. Trömel, and C. Simmer, 2020: Comparison between precipitation estimates of ground-based weather radar composites and GPM's DPR rainfall product over Germany. *Meteor. Z.*, **29**, 451–466, https://doi.org/10.1127/metz/2020/1039.

——, J. Soderholm, K. Mühlbauer, V. Louf, and S. Trömel, 2022: Five years of calibrated measurements of the polarimetric X-band weather radar in Bonn (BoXPol). *Sci. Data*, **9**, 551, https://doi.org/10.1038/s41597-022-01656-0.

Probert-Jones, J. R., 1962: The radar equation in meteorology. *Quart. J. Roy. Meteor. Soc.*, **88**, 485–495, https://doi.org/10.1002/qj.49708837810.

Protat, A., D. Bouniol, E. J. O'Connor, H. Klein Baltink, J. Verlinde, and K. Widener, 2011: *CloudSat* as a global radar calibrator. *J. Atmos. Oceanic Technol.*, **28**, 445–452, https://doi.org/10.1175/2010JTECHA1443.1.

——, V. Louf, J. Soderholm, J. Brook, and W. Ponsonby, 2022: Three-way calibration checks using ground-based, ship-based and spaceborne radars. *Atmos. Meas. Tech.*, **15**, 915–926, https://doi.org/10.5194/amt-15-915-2022.

Richardson, L. M., J. G. Cunningham, W. D. Zittel, R. R. Lee, R. L. Ice, V. M. Melnikov, N. P. Hoban, and J. G. Gebauer, 2017a: Bragg scatter detection by the WSR-88D. Part I:

Algorithm development. *J. Atmos. Oceanic Technol.*, **34**, 465–478, https://doi.org/10.1175/JTECH-D-16-0030.1.

——, W. D. Zittel, R. R. Lee, V. M. Melnikov, R. L. Ice, and J. G. Cunningham, 2017b: Bragg scatter detection by the WSR-88D. Part II: Assessment of $Z_{DR}$ bias estimation. *J. Atmos. Oceanic Technol.*, **34**, 479–493, https://doi.org/10.1175/JTECH-D-16-0031.1.

Rinehart, R. E., 1978: On the use of ground return targets for radar reflectivity factor calibration checks. *J. Appl. Meteor.*, **17**, 1342–1350, https://doi.org/10.1175/1520-0450(1978)017<1342:OTUOGR>2.0.CO;2.

Ryzhkov, A. V., S. E. Giangrande, V. M. Melnikov, and T. J. Schuur, 2005: Calibration issues of dual-polarization radar measurements. *J. Atmos. Oceanic Technol.*, **22**, 1138–1155, https://doi.org/10.1175/JTECH1772.1.

Saltikoff, E., and Coauthors, 2019: OPERA the radar project. *Atmosphere*, **10**, 320, https://doi.org/10.3390/atmos10060320.

Sanchez-Rivas, D., and M. Rico-Ramirez, 2022: Calibration of radar differential reflectivity using quasi-vertical profiles. *Atmos. Meas. Tech.*, **15**, 503–520, https://doi.org/10.5194/amt-15-503-2022.

Scarchilli, G., V. Gorgucci, V. Chandrasekar, and A. Dobaie, 1996: Self-consistency of polarization diversity measurement of rainfall. *IEEE Trans. Geosci. Remote Sens.*, **34**, 22–26, https://doi.org/10.1109/36.481887.

Schwaller, M. R., and K. R. Morris, 2011: A ground validation network for the Global Precipitation Measurement mission. *J. Atmos. Oceanic Technol.*, **28**, 301–319, https://doi.org/10.1175/2010JTECHA1403.1.

Silberstein, D. S., D. B. Wolff, D. A. Marks, D. Atlas, and J. L. Pippitt, 2008: Ground clutter as a monitor of radar stability at Kwajalein, RMI. *J. Atmos. Oceanic Technol.*, **25**, 2037–2045, https://doi.org/10.1175/2008JTECHA1063.1.

Stephens, G. L., and Coauthors, 2002: The *CloudSat* mission and the A-Train. *Bull. Amer. Meteor. Soc.*, **83**, 1771–1790, https://doi.org/10.1175/BAMS-83-12-1771.

Toyoshima, K., H. Masunaga, and F. A. Furuzawa, 2015: Early evaluation of Ku- and Ka-band sensitivities for the Global Precipitation Measurement (GPM) Dual-Frequency Precipitation Radar (DPR). *SOLA*, **11**, 14–17, https://doi.org/10.2151/sola.2015-004.

Truong, C., L. Oudre, and N. Vayatis, 2020: Selective review of offline change point detection methods. *Signal Process.*, **167**, 107299, https://doi.org/10.1016/j.sigpro.2019.107299.

Vaccarono, M., R. Bechini, C. V. Chandrasekar, R. Cremonini, and C. Cassardo, 2016: An integrated approach to monitoring the calibration stability of operational dual-polarization radars. *Atmos. Meas. Tech.*, **9**, 5367–5383, https://doi.org/10.5194/amt-9-5367-2016.

Wang, J., and D. B. Wolff, 2009: Comparisons of reflectivities from the TRMM Precipitation Radar and ground-based radars. *J. Atmos. Oceanic Technol.*, **26**, 857–875, https://doi.org/10.1175/2008JTECHA1175.1.

Warren, R. A., A. Protat, S. T. Siems, H. A. Ramsay, V. Louf, M. J. Manton, and T. A. Kane, 2018: Calibrating ground-based radars against TRMM and GPM. *J. Atmos. Oceanic Technol.*, **35**, 323–346, https://doi.org/10.1175/JTECH-D-17-0128.1.

——, H. A. Ramsay, S. T. Siems, M. J. Manton, J. R. Peter, A. Protat, and A. Pillalamarri, 2020: Radar-based climatology of damaging hailstorms in Brisbane and Sydney, Australia. *Quart. J. Roy. Meteor. Soc.*, **146**, 505–530, https://doi.org/10.1002/qj.3693.

Whiton, R. C., P. L. Smith, and A. C. Harbuck, 1976: Calibration of weather radar systems using the sun as a radio source. *17th Conf. on Radar Meteorology*, Seattle, WA, Amer. Meteor. Soc., 60–65.

WMO, 2018: Guide to meteorological instruments and methods of observation. WMO Doc. WMO-8, 133 pp., https://library.wmo.int/doc_num.php?explnum_id=9869.

Wolff, D. B., D. A. Marks, and W. A. Petersen, 2015: General application of the relative calibration adjustment (RCA) technique for monitoring and correcting radar reflectivity calibration. *J. Atmos. Oceanic Technol.*, **32**, 496–506, https://doi.org/10.1175/JTECH-D-13-00185.1.